

# Galaxy density profiles and shapes – II. selection biases in strong lensing surveys

Rachel Mandelbaum<sup>1\*</sup>, Glenn van de Ven<sup>1†</sup>, Charles R. Keeton<sup>2‡</sup>

<sup>1</sup>*Institute for Advanced Study, Einstein Drive, Princeton NJ 08540, USA*

<sup>2</sup>*Department of Physics and Astronomy, Rutgers University, 136 Frelinghuysen Road, Piscataway NJ, 08854, USA*

30 October 2018

## ABSTRACT

Many current and future astronomical surveys will rely on samples of strong gravitational lens systems to draw conclusions about galaxy mass distributions. We use a new strong lensing pipeline (presented in Paper I of this series) to explore selection biases that may cause the population of strong lensing systems to differ from the general galaxy population. Our focus is on point-source lensing by early-type galaxies with two mass components (stellar and dark matter) that have a variety of density profiles and shapes motivated by observational and theoretical studies of galaxy properties. We seek not only to quantify but also to understand the physics behind selection biases related to: galaxy mass, orientation and shape; dark matter profile parameters such as inner slope and concentration; and adiabatic contraction. We study how all of these properties affect the lensing Einstein radius, total cross-section, quad/double ratio, and image separation distribution, with a flexible treatment of magnification bias to mimic different survey strategies. We present our results for two families of density profiles: cusped and deprojected Sérsic models. While we use fixed lens and source redshifts for most of the analysis, we show that the results are applicable to other redshift combinations, and we also explore the physics of how our results change for very different redshifts. We find significant (factors of several) selection biases with mass; orientation, for a given galaxy shape at fixed mass; cusped dark matter profile inner slope and concentration; concentration of the stellar and dark matter deprojected Sérsic models. Interestingly, the intrinsic shape of a galaxy does not strongly influence its lensing cross-section when we average over viewing angles. Our results are an important first step towards understanding how strong lens systems relate to the general galaxy population.

**Key words:** gravitational lensing – galaxies: photometry – galaxies: structure – galaxies: elliptical and lenticular – galaxies: fundamental parameters

## 1 MOTIVATION

The field of strong lensing is undergoing a period of growth that is expected to accelerate in the coming decade. Current samples with tens of lenses, such as from CASTLES<sup>1</sup> (e.g., Falco et al. 2001), CLASS (e.g., Browne et al. 2003), SDSS (e.g., Inada et al. 2008), and SLACS (e.g., Bolton et al. 2008), will give way to samples with hundreds or even thousands of strong lensing systems discovered by Pan-STARRS, LSST, SNAP, and SKA (e.g.,

Fassnacht et al. 2004; Koopmans et al. 2004; Kuhlen et al. 2004; Marshall et al. 2005). As lens samples grow, they will be even more useful for constraining the mass distributions of the strong lensing galaxy population (for a review of strong lensing astrophysics, see Kochanek 2006).

There are, however, certain complications in using strong lensing studies to constrain the physical properties of galaxies. The issue we address here is *selection bias*. Suppose we treat galaxies as having an intrinsic probability distribution in some parameter  $x$  (such as the inner slope of the density profile), and we want to use observed strong lens systems to infer that distribution  $p(x)$ . If the lensing probability itself depends on  $x$ , then in general the distribution  $p_{\text{SL}}(x)$  for the strong lens galaxies will not reflect the true, underlying  $p(x)$  for all galaxies. The more diverse the galaxy population, and the more the strong lensing cross-

\* rmandelb@ias.edu, Hubble Fellow

† glenn@ias.edu, Hubble Fellow

‡ keeton@physics.rutgers.edu

<sup>1</sup> CASTLES is a collection of uniform HST observations of mostly point-source lenses from several samples with differing selection criteria, rather than a single, uniformly-selected survey.

section varies across the population, the more important the selection biases can be.

Obviously, one must account for selection biases in order to draw reliable conclusions from current and future strong lens samples. Our purpose here is to use a complete, end-to-end, and above all, realistic simulation pipeline for strong lensing (presented in Paper I of this series, van de Ven, Mandelbaum, & Keeton 2008) to quantify and understand strong lensing selection biases and assess their impact in typical situations. We focus on strong lensing of quasars by early-type, central (non-satellite) galaxies at several mass scales, using two-component mass profiles (dark matter plus stars) that are consistent with existing photometry and stacked weak lensing data from SDSS (Kauffmann et al. 2003; Mandelbaum et al. 2006) as well as with  $N$ -body and hydrodynamic simulations.

The issue of selection biases in strong lensing is not a new one, and we are building on many previous studies of this issue. The main galaxy properties that we study in an attempt to understand selection bias are

- Mass (e.g., Turner et al. 1984; Fukugita & Turner 1991; Möller et al. 2007);
- Orientation (“inclination bias”, e.g., Maller et al. 1997; Keeton & Kochanek 1998; Rozo et al. 2007);
- Shape (e.g., Keeton et al. 1997; Huterer et al. 2005; Rozo et al. 2007);
- Dark matter inner slope (e.g., Keeton & Madau 2001; Wyithe et al. 2001; Li & Ostriker 2002);
- Dark matter concentration (e.g., Kuhlen et al. 2004; Fedeli et al. 2007).

In most cases, previous studies addressed the issue of selection bias using models that were simplified in some way. Simplifications often included testing effects of dark matter slope and concentration using pure (generalised) NFW profiles without a baryonic component; or testing effects of density profile or shape using single-component mass models. A notably different approach was taken by Hilbert et al. (2007), Möller et al. (2007), and Hilbert et al. (2008), who used the Millennium simulation with a semi-analytic model of galaxy formation to simulate strong lensing. That approach naturally yields a realistic distribution of halo and galaxy properties (to the extent that the true distribution of galaxy properties and their relation to halo properties is encoded in the semi-analytic model), at least for a fixed cosmological model, and it will undoubtedly be useful for modeling the strong lensing population in large, future surveys. We elect, however, to take a more controlled approach here, using realistic but discrete values of the density profile parameters, so that we can disentangle the different types of lensing selection biases, and understand the physics of each one, before recombining them to determine the net effects.

Our basic approach is to generate realistic galaxy models with various values of the relevant parameters, and to investigate how the lensing cross-section  $\sigma(\vec{x})$  depends on model parameters  $\vec{x}$  (where  $\vec{x}$  might include mass, shape, concentration, and other parameters, some of which may be correlated). The reason for focusing on the cross-section is that it represents the weighting factor that transforms the intrinsic joint parameter distribution  $p(\vec{x})$  into the distribution  $p_{\text{SL}}(\vec{x})$  among observed strong lens systems. Note that we focus on selection biases related to *physical* effects. There

may also be *observational* selection biases (e.g., Kochanek 1991), but they are specific to a given survey and are not something that we can address in a general way. This fact is one reason for our focus on point-source lensing: extended source lensing is even more sensitive to observational selection effects than quasar lensing. For example, the effect of a finite aperture is no longer straightforward for an extended source, and detection of an extended strong lens system depends on factors such as the size of the point-spread function which varies spatially and temporally in any given survey. Fortunately, with large numbers of point-source lens systems anticipated in future surveys [e.g.,  $\sim 10^5$  with SKA (Koopmans et al. 2004)] this investigation of physical selection biases in point-source lens systems should be highly useful. We emphasize that our purpose is only to determine the mapping function  $\sigma(\vec{x})$  due to physical differences between galaxies, and not to predict the observed distribution of properties  $p_{\text{SL}}(\vec{x})$  in some particular lensing survey, for which knowledge of the intrinsic parameter distribution  $p(\vec{x})$  and of any observational selection effects are both necessary.

In this paper, we present a systematic investigation of physical strong lensing selection biases that both unifies and extends previous work. We begin in Section 2 with a brief review of the simulation pipeline developed in Paper I, including the density profiles and shapes of our galaxy models, our computational lensing methods, and the basic lensing properties of our galaxies. In Section 3, we investigate selection biases related to galaxy orientation and shape. In Section 4, we consider selection biases related to the inner slope of the dark matter component of the density profile (for cusped models). In Section 5, we allow the dark matter concentration to vary as well. In Section 6, we turn to de-projected Sérsic density profiles and examine selection biases with both the stellar and dark matter parameters. Section 7 includes an exploration of the ranges of lens and source redshifts for which our conclusions are applicable. Finally, in Section 8, we summarise our main conclusions and discuss their implications for past and future strong lensing analyses.

## 2 SIMULATIONS

Here we summarise the strong lensing simulation pipeline that was developed in Paper I. For more details regarding the choice of galaxy models, and the lensing calculations (including validation and convergence tests), we refer the reader to that paper.

### 2.1 Notation and conventions

The pipeline assumes fiducial lens and source redshifts of  $z_L = 0.3$  and  $z_S = 2.0$ , respectively, although we explore a range of lens and source redshifts in Section 7. We compute distances using a flat  $\Lambda$ CDM cosmology with  $\Omega_m = 0.27$  and  $h = 0.72$ . With these choices, the angular scale at the lens redshift is  $1'' = 4.36$  kpc and the lensing critical density is  $\Sigma_c = 2389 M_\odot \text{pc}^{-2}$ .

We use  $x$ ,  $y$ , and  $z$  to denote intrinsic, three-dimensional (3d) coordinates, and  $x'$  and  $y'$  for the projected, two-dimensional (2d) coordinates. Similarly,  $r$  is the intrinsic radius ( $r^2 = x^2 + y^2 + z^2$ ) and  $R'$  is the projected radius

( $R'^2 = x'^2 + y'^2$ ). For non-spherical galaxies, we use  $a$ ,  $b$ , and  $c$  for the major, intermediate, and minor semi-axis lengths of the intrinsic, 3d density profiles; and we use  $a'$  and  $b'$  for the major and minor semi-axis lengths of the projected, 2d surface densities. Subscripts “dm” and “ $\star$ ” are used to indicate whether a quantity describes the dark matter (DM) or stellar component of the galaxy model. Any gas component that has not cooled to form stars — which is expected to be sub-dominant relative to the stellar component for early type galaxies (e.g., Read & Trentham 2005; Morganti et al. 2006) — is implicitly included in the component that we label dark matter.

All quoted dark matter masses  $M_{180}$  are defined using comoving quantities such that the average density within the virial radius is  $180\bar{\rho}$ . This definition is in principle arbitrary, but this choice was used to analyse the weak lensing results that we use to estimate masses for our galaxy models.

## 2.2 Galaxy models

Our guiding principle in designing the galaxy models and choosing their parameters is that we want them to be realistic examples of galaxies, but not necessarily to reproduce the full intrinsic parameter distribution of real galaxies. The reason for the latter point is that strong lensing is inherently non-linear, so it may be the case that a region of parameter space with very few galaxies is actually quite important for strong lensing because it has a large cross-section. A classic example is brightest cluster galaxies, which are a negligible fraction of the galaxy population, yet constitute a non-negligible fraction of strong lenses. Consequently, we choose parameter values taking into account prior knowledge of the intrinsic parameter distributions —where known— and using physical intuition for what effects may strongly increase the lensing cross-section, such as a steep inner slope of the dark matter density.

### 2.2.1 Basic setup

All of the ellipsoidal galaxy models used for this pipeline involve two components, one for the stars and one for the dark matter. The parameters of stellar components are based on photometry and spectroscopy from the SDSS (Kauffmann et al. 2003). The parameters of the dark matter components are derived from  $N$ -body simulations and stacked weak lensing observations of early-type galaxies in SDSS (Mandelbaum et al. 2006). We attempt to approximately bracket the range of luminosities of observed strong lensing systems by using models corresponding to  $\sim 2L_\star$  and  $\sim 7L_\star$  early-type, central (non-satellite) lens galaxies. (See, e.g., Keeton & Zabludoff 2004 and Momcheva et al. 2006 for a discussion of environmental effects when the lens galaxy is a satellite in a group or cluster of galaxies.) The derivation of the resulting mass and length scales is explained in Paper I.

Here we briefly mention that the stellar components have masses  $M_{\text{tot},\star}$  of 1.16 and  $5.6 \times 10^{11} M_\odot$ , and projected half-mass radii  $R'_{h,\star}$  of 4.07 and 11.7 kpc for the above lower (“galaxy”) and higher (“group”) mass scale, respectively. The dark matter components have halo masses  $M_{180,\text{dm}}$  of 0.47 and  $9.3 \times 10^{13} M_\odot$ , and concentrations  $c_{\text{dm}}$  of 8.4 and

5.6, which implies scale radii  $r_{s,\text{dm}}$  of 49.7 and 201 kpc, for the lower and higher mass scale, respectively. We note that a simulation with only two mass models is not sufficient for a fully quantitative study of mass bias in strong lensing. We have limited the number of mass models because mass bias is among the oldest and best-studied selection effects in strong lensing, so we focus instead on other effects for which the answers are less clear.

### 2.2.2 Density profiles

We use two basic types of density profiles for the simulation pipeline. The first are cusped density profiles, which have the general form

$$\rho(r) = \frac{\rho_0}{m^\gamma(1+m)^{n-\gamma}}, \quad (1)$$

where  $m$  is a dimensionless ellipsoidal radius; in the spherical case,  $m = r/r_s$  for some scale radius  $r_s$ . For the stellar cusped density, we use the Hernquist (1990) profile, which has  $(\gamma, n) = (1, 4)$ . For the cusped density of the DM halo, we use the NFW (Navarro et al. 1997) profile, which has  $(\gamma, n) = (1, 3)$ , but generalise it by allowing  $\gamma$  to vary on a grid of values  $\{0.5, 1, 1.5\}$ . Further variation of the cusped models includes several simulations with adiabatic contraction of the DM halo due to the presence of the stellar component, according to the prescriptions given in Blumenthal et al. (1986) and Gnedin et al. (2004).

The second type of profile that we use is a deprojected Sérsic (1968) profile, which is well-described using the formula from Prugniel & Simien (1997),

$$\rho(m) = \frac{\rho_0}{m^{p_n}} \exp\left[-b_n m^{1/n}\right], \quad (2)$$

where the central (negative) logarithmic slope is related to the Sérsic index  $n$  by  $p_n = 1 - 0.6097/n + 0.05563/n^2$ , and  $b_n = 2n - 1/3 + 4/(405n) + 46/(25515n^2)$  to high precision (Ciotti & Bertin 1999). The scale radius is the projected half-mass radius, which in case of a constant stellar mass-to-light ratio corresponds to the effective radius  $R_e$ . The Sérsic indices  $n_\star$  of the stellar component from observational constraints (Ferrarese et al. 2006) and  $n_{\text{dm}}$  of the dark matter component from  $N$ -body simulations (Merritt et al. 2005) are 4.29 and 2.96 (respectively) for the lower mass scale, and 5.87 and 2.65 for the higher mass scale. We also investigate varying both  $n_{\text{dm}}$  and  $n_\star$  away from these fiducial values within the ranges derived in Paper I.

Paper I includes a number of figures characterising the intrinsic (3d) and projected (2d) density profiles of our model galaxies. We highlight the following projected quantities (since the projected mass distribution is what governs lensing): the surface mass density  $\Sigma(R')$  (figure 4); the negative logarithmic slope  $\gamma'(R')$  of the surface mass density (figure 5); the projected enclosed dark matter fraction  $f'_{\text{dm}}(R')$  (figure 6); and the lensing deflection angle  $\alpha(R')$  (figure 7). Those quantities are plotted for both the cusped and deprojected Sérsic density profiles at both mass scales.

One characteristic of these galaxy models that was noted in Paper I, and that will be important in our interpretation of results in this paper, is that from  $\sim 1$ –50 kpc (cusped models) or from  $\sim 0.3$ –30 kpc (deprojected Sérsic models), the composite galaxy model is approximately isothermal. This result can be most easily seen in Paper I

figures 5 and 7. Moreover, it is still nearly true not only for our fiducial models but for our models with varying  $\gamma_{\text{dm}}$  (cusped) or  $n_{\text{dm}}$  and  $n_*$  (Sérsic). For the higher mass models, the deviations from isothermality are more significant.

While we will find later on that the deviations from isothermality on small scales, well within  $R_{\text{ein}}$ , can have noticeable effects for the lensing properties (e.g., the relationship between the Einstein radius and the total unbiased cross section differs from the relation  $\sigma = \pi R_{\text{ein}}^2$  that applies to singular isothermal spheres), we can nonetheless use this approximate result to reason about selection biases with certain galaxy properties. For example, steeper dark matter inner slopes  $\gamma_{\text{dm}}$  and higher concentrations  $c_{\text{dm}}$ ,  $n_{\text{dm}}$ , or  $n_*$  mean that a larger fraction of the total galaxy mass (stellar plus dark) is located within some fixed aperture. When combining this fact with the approximate isothermality, we can envision the profile on those scales as simply being increased by a multiplicative factor when we increase  $\gamma_{\text{dm}}$ ,  $c_{\text{dm}}$ ,  $n_{\text{dm}}$ , or  $n_*$ . Consequently, higher values of these parameters increase the total lensing cross-section, and in the case of  $\gamma_{\text{dm}}$ ,  $c_{\text{dm}}$ , and  $n_{\text{dm}}$ , they also increase the projected dark matter fraction  $f'_{\text{dm}}$  in the inner regions.

### 2.2.3 Shape models

We consider seven different models for the shape of the galaxy density: spherical, moderately oblate, very oblate, moderately prolate, very prolate, triaxial, and a mixed model. In all but the mixed model, the axis ratios used for the dark matter and stellar components are related in a simple way (with the stellar component being slightly rounder than the dark matter component). In all cases the axes of the two components are intrinsically aligned. The mixed model includes an oblate stellar component that has short axis aligned with the short axis of a triaxial dark matter halo. The chosen axis ratios for all models, and the method of sampling in viewing angle to compute accurate orientation-averaged lensing cross-sections, are given in Paper I.

### 2.3 Strong lensing calculations

Here we briefly summarise the strong lensing calculations, which are described in far greater detail in Paper I. In all cases, we consider only point-source (quasar) lensing, and do all calculations using an updated version of the GRAVLENS software package (Keeton 2001b).

For the cusped models, we compute the scaled surface mass density  $\kappa = \Sigma/\Sigma_c$  on a map, and use Fourier transforms to solve the Poisson equation and find the lens potential. We then compute the first and second real-space derivatives of the potential in Fourier space, and use inverse FFTs to transform back to real space. Paper I presents tests to determine what map resolution and size are necessary to avoid numerical errors in the Fourier analysis. With deprojected Sérsic models it is hard for the map-based approach to resolve the steep central profile, so we instead compute the lensing deflection and magnification analytically (for spherical models; also see Cardone 2004; Baltz et al. 2009), or with numerical integrals (for non-spherical models).

We use the routine `calcRein` to calculate the Einstein radius  $R_{\text{ein}}$  for general density distributions, and the routine `mockcsec` to compute strong lensing cross-sections using

Monte Carlo techniques. Specifically, `mockcsec` places many random sources behind the lens, solves the lens equation to find all the images, and then tabulates the cross-sections for lensing with different numbers of images (2, 3, or 4).<sup>2</sup> We can add those cross-sections to find the total lensing cross-section,  $\sigma_{\text{tot}}$ . We use bootstrap resampling to estimate the statistical uncertainties in the cross-sections.

We account for magnification bias in various ways intended to mimic different survey strategies. We use the GRAVLENS routine `mockLF` to define an observationally-motivated double-power-law luminosity function for the source quasar population; and we consider surveys with faint, intermediate and high flux limits (ranging from locally shallow to locally steep parts of the luminosity function: 0.04, 0.4, and  $4L_*$ ). We compute magnification bias using either the total magnification of all images, which is appropriate for surveys that do not initially resolve strong lens systems, and separately, using the magnification of the second-brightest image (for surveys with sufficient resolution to resolve strong lens systems from the outset). All told, we examine six types of biased cross-sections in addition to the unbiased lensing cross-section.

### 2.4 Basic results

Here, we present the basic lensing properties of our spherical cusped galaxy models. Table 1 gives the Einstein radii and unbiased lensing cross-sections ( $\sigma_{\text{tot}} = \sigma_2$  for spherical models) for models at both mass scales, for different values of the dark matter inner slope  $\gamma_{\text{dm}}$ .

There are three points to note about these results. First, the strong lensing properties are, as expected, a strong function of mass. For the fiducial dark matter inner slope  $\gamma_{\text{dm}} = 1$ , the Einstein radius  $R_{\text{ein}}$  and lensing cross-section increase by factors of 2.6 and 3.1 when we go from the lower to the higher mass model; for  $\gamma_{\text{dm}} = 1.5$ , the factors of 4.3 and 10.7 increase are even larger. Our results are broadly consistent with conclusions by Turner et al. (1984), Fukugita & Turner (1991), Möller et al. (2007) and from many other studies that the population of lens galaxies differs from the overall galaxy population in its overall higher mean stellar and DM halo mass. The higher mean mass for the strong lensing systems is determined by the competition between the rising  $\sigma_{\text{tot}}$  with mass and the steeply declining mass function at high masses. A second point is that the increase in  $\sigma_{\text{tot}}$  with mass is notably larger for the models with  $\gamma_{\text{dm}} = 1.5$  than for the models with  $\gamma_{\text{dm}} = 1$ . This means the strong lensing mass bias depends sensitively on the inner slope of the intrinsic density profile. A third point is that, even when the mass is fixed,  $R_{\text{ein}}$  and  $\sigma_{\text{tot}}$  are very sensitive to  $\gamma_{\text{dm}}$ . While this is not surprising, the latter two points do serve as a reminder that calling strong lens galaxies a “mass-selected” sample of galaxies is an over-simplification.

<sup>2</sup> In each 2-image and 4-image system, there is actually one additional image that lies near the centre of the lens galaxy (so in some of the lensing literature such systems are called 3-image and 5-image systems instead). The central images are highly demagnified and rarely observed, however, which is why most observed lenses are considered to be doubles and quads. We do find the central images but do not include them in our astrophysical analysis. See Paper I for more discussion.

**Table 1.** Summary of the basic lensing results for the spherical shape model.

Description	Lower mass				Higher mass			
	$\gamma_{\text{dm}} = 0.5$	$\gamma_{\text{dm}} = 1$	$\gamma_{\text{dm}} = 1.5$	SIS	$\gamma_{\text{dm}} = 0.5$	$\gamma_{\text{dm}} = 1$	$\gamma_{\text{dm}} = 1.5$	SIS
$R_{\text{ein}}$ (kpc)	2.5	3.0	4.5	2.4	5.1	7.6	19.4	17.3
$R_{\text{ein}}$ (arcsec)	0.58	0.68	1.04	0.55	1.18	1.75	4.44	3.97
$\sigma_{\text{tot}}$ (arcsec <sup>2</sup> ), unbiased	0.42	0.53	1.40	0.95	0.84	1.63	15.0	49.5

As a reference point, we also consider a single-component singular isothermal sphere (SIS) model which has the same mass within the virial radius as our two-component galaxy models (for each mass scale). Even if the density profile is truncated at the virial radius, for radii well inside the virial radius the intrinsic density profile can be given as  $\rho_{\text{SIS}}(r) = M_{180}/(4\pi r_{180}^2 r^2)$ , and the surface density as  $\Sigma(R') \simeq M_{180}/(4r_{180}R')$ . To find the Einstein radius, we require for the mean surface brightness that  $\bar{\Sigma}(R_{\text{ein}}) = \Sigma_c$ , which gives

$$R_{\text{ein}}^{(\text{SIS})} = \frac{M_{180}}{2r_{180}\Sigma_c} \propto M_{180}^{2/3} \quad (3)$$

where  $M_{180}$  and  $r_{180}$  are related by our virial mass definition,

$$\frac{3M_{180}}{4\pi r_{180}^3} = 180\bar{\rho} \quad (4)$$

The resulting Einstein radii and lensing cross-sections ( $\sigma_{\text{tot}} = \pi R_{\text{ein}}^2$ ) are also given in Table 1.

Comparing the familiar SIS model with our more complex, two-component models yields some notable results. For the lower mass scale, the SIS Einstein radius is similar to that of our shallow  $\gamma_{\text{dm}} = 0.5$  cusped model, but the SIS cross-section lies between those of the steeper  $\gamma_{\text{dm}} = 1$  and  $\gamma_{\text{dm}} = 1.5$  cusped models. For the higher mass scale, the SIS Einstein radius  $R_{\text{ein}}^{(\text{SIS})}$  is only slightly smaller than that for the  $\gamma_{\text{dm}} = 1.5$  cusped model, and the SIS cross-section is considerably higher than that for any of our cusped models. This result can be understood from paper I figure 5, which shows that while  $\gamma'$  for our lower mass models is near the SIS value of  $\gamma' = 1$  near  $R_{\text{ein}}$ , it is significantly shallower for a fair fraction of the range inside  $R_{\text{ein}}$ . The shallower inner slope moves the (source-plane) radial caustic inwards, decreasing the cross-section to well below the SIS value of  $\pi R_{\text{ein}}^2$ .

One implication is that a simple SIS model cannot mimic any particular one of our cusped models. Thus, even though galaxies seem to have quasi-isothermal profiles in the vicinity of the Einstein radius (see Paper I), a simple SIS is still not very realistic as a *global* lens model. The difference between the SIS and more complex two-component lens models is particularly notable on mass scales corresponding to groups of galaxies and above (also see Keeton 1998; Porciani & Madau 2000; Kochanek & White 2001; Kuhlen et al. 2004).

### 3 ORIENTATION AND SHAPE

We begin our main science results by examining selection biases as a function of galaxy orientation and shape, for fixed dark matter inner slope  $\gamma_{\text{dm}}$ . In Section 3.1 we investigate ‘‘orientation bias’’ for each of the six non-spherical shape

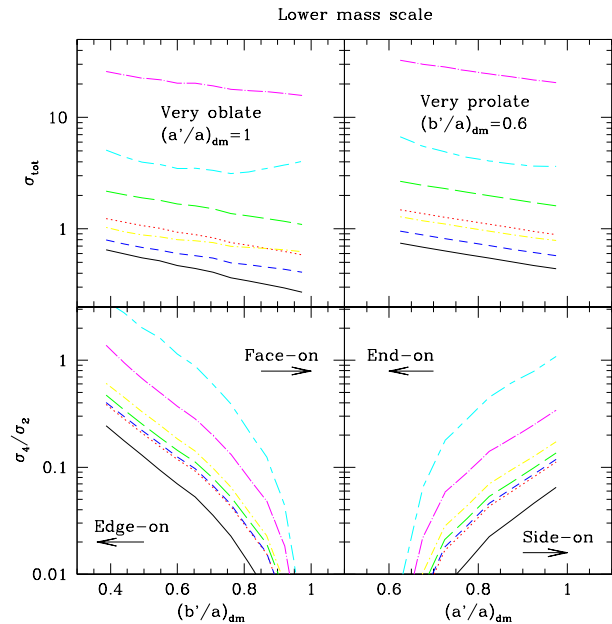


**Figure 1.** The total lensing cross-section  $\sigma_{\text{tot}}$  (top) and quad/double ratio (bottom) as a function of projected semi-axis lengths for the lower mass cusped model for very oblate (left) and very prolate (right) shapes. The lines indicate magnification bias modes as follows: black solid = unbiased, red dotted and blue dashed = weighted by total and second-brightest magnification respectively for  $0.04L_*$  limiting magnitude, green long-dashed and yellow dot-dashed = the same for  $0.4L_*$  limiting magnitude, and magenta dot-long dashed and cyan short-long dashed = the same for  $4L_*$  limiting magnitude.

models. In Section 3.2 we consider orientation-averaged cross-sections for all model shapes, to see if there are significant selection biases associated with the *intrinsic* shapes of galaxies. Finally, in Section 3.3 we consider whether there is any simple, universal conversion between unbiased and biased lensing cross-sections.

#### 3.1 Orientation

In this subsection, we fix the dark matter inner slope to  $\gamma_{\text{dm}} = 1$  and examine how the orientation of non-spherical models affects their lensing cross-sections (‘‘orientation bias’’). Our basic physical intuition suggests the following trends with orientation for a given shape:

(i) When viewing the galaxy along the long axis (with scale length  $a$ ), the projected scale radii are minimised, so that the most mass is squeezed into the smallest projected area. The resulting higher surface density at fixed  $R'$  im-

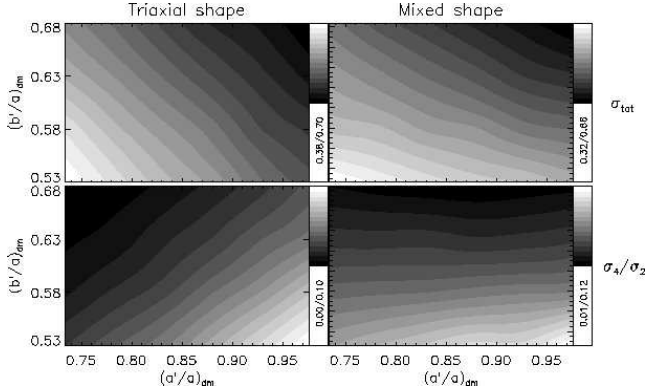


**Figure 2.** Contour plots of the total lensing cross-sections  $\sigma_{\text{tot}}$  (top) and quad/double ratios (bottom) as a function of projected semi-axis lengths for the lower mass cusped model for triaxial (left) and mixed (right) shapes, where the axis labels indicate the shape of the dark matter component. All quantities are unbiased cross-sections only.

plies an increased Einstein radius and higher lensing cross-section.

(ii) The four-image cross-section  $\sigma_4$  and the quad/double ratio  $\sigma_4/\sigma_2$  increase with the projected ellipticity; they are maximised when viewing the halo along the intermediate axis, such that the long and short axes are seen in projection (i.e., projected axis ratio  $b'/a' = c/a$ ). The four-image cross-section vanishes when the projected surface density has circular symmetry, i.e., for an oblate galaxy viewed face-on or a prolate galaxy viewed end-on.

(iii) The three-image cross-sections can only be significant in cases of extreme projected ellipticity, when the tangential caustic protrudes outside the radial caustic.

We first consider the very oblate and very prolate models. Fig. 1 shows the total cross-section  $\sigma_{\text{tot}}$  and the quad/double ratio  $\sigma_4/\sigma_2$  for the lower mass scale (results for the higher mass scale are similar). The total cross-section is indeed higher for oblate models viewed edge-on rather than face-on, and for prolate models viewed end-on rather than side-on (i.e., viewed with the long axis along the line-of-sight in each case). The total cross-section varies with orientation by factors of  $\sim 2$  for these strongly non-spherical models; in the higher mass model (not shown), the variation is as much as a factor of 4 because the flatter DM component is more prominent. This finding implies that if strong lensing systems seen in reality are drawn from significantly non-spherical galaxies, we should observe preferential alignment of the long axis with the line-of-sight, rather than random orientations.

The cross-sections for three- and four-image systems behave in accordance with our expectations. As can be seen from  $\sigma_4/\sigma_2$  in the bottom panels of Fig. 1, four-image systems are plentiful for orientations that yield a large projected ellipticity — for oblate galaxies viewed edge-on, or prolate galaxies viewed side-on — but they naturally disappear as the projected mass density approaches circularity. While we have not plotted  $\sigma_3$  since in most cases it is zero, we see substantial numbers of three-image systems only for edge-on oblate galaxies, where the projected matter density is so flat that the tangential caustic protrudes beyond the

radial caustic. Above some critical projected axis ratio,  $\sigma_3$  becomes consistent with zero.

Magnification bias increases the effective cross-sections, because lensing magnification brings in systems that would have been below the flux limit had they not been lensed. The effect is strongest when the flux limit is in the steep part of the source luminosity function (the  $4L_*$  limiting luminosity). In all cases, the biased cross-section is larger when calculated using the total magnification rather than the magnification of the second-brightest image, but the trends with viewing angle are typically preserved. The  $\sigma_4/\sigma_2$  ratio is increased by magnification bias, because four-image lenses tend to have higher magnifications than two-image lenses. This ratio increases with the flux limit, but it is actually higher when using the second-brightest magnification rather than the total magnification, because many four-image lenses have at least two bright images. We discuss further details of the biased cross-sections in Section 3.3.

Next, we consider the more complex triaxial and mixed shape models shown in Fig. 2. For both mass scales, the total cross-sections have maxima when  $a'/a = b/a$  and  $b'/a = c/a$  (i.e., the projected semi-axis lengths have their minimum values), which corresponds to the long axis being along the line-of-sight. This result is therefore physically intuitive, and consistent with the results in Rozo et al. (2007) for single-component isothermal ellipsoid lens models. The total variation of  $\sigma_{\text{tot}}$  with viewing angle for these typical triaxial models is a factor of  $\sim 2$  at the lower mass scale, or as much as 4 in the higher mass case (where the flatter DM component contributes more). The  $\sigma_4/\sigma_2$  ratio reaches its maximum value when  $a'/a = 1$  (maximum value) and  $b'/a = c/a$  (minimum value), which corresponds to the most flattened projected mass distribution. In the mixed case, the orientation of the oblate stellar component is such that, regardless of  $(a'/a)_{\text{dm}}$ , the top of the plot corresponds to a rounder projected stellar density because it is seen face-on, while the bottom of the plot corresponds to a flatter projected stellar density because it is seen edge-on, so that both  $\sigma_{\text{tot}}$  and  $\sigma_4/\sigma_2$  increase from top to bottom. As a result, the trends in both  $\sigma_{\text{tot}}$  and  $\sigma_4/\sigma_2$  are not significantly modified from the triaxial case, except for a tilt in the contours which can be accounted for by considering the orientation of the oblate stellar component.

We conclude that strong lenses drawn from a parent population with randomly-oriented non-spherical matter distributions have a projected axis ratio distribution that is not consistent with that of a random sample of the population, because there are preferred orientations for the lensing systems. The degree of preference for particular orientations can be factors of several depending on the intrinsic axis ratios, the relative contribution of the flatter DM component, and the number of images in the lenses being considered. While it is difficult to compare quantitatively with the conclusions of previous works on “inclination bias” (e.g., Maller et al. 1997; Keeton & Kochanek 1998; Rozo et al. 2007) due to the very different mass models used, qualitatively we agree with the results that for an intrinsically non-spherical model, orientation effects are important at this level. In particular, the trends we find regarding  $\sigma_{\text{tot}}$  and  $\sigma_4/\sigma_2$  for triaxial models agree well with those of Rozo et al. (2007).

The preceding discussion has used results for fixed dark matter inner slope  $\gamma_{\text{dm}} = 1$ . Generally, we find that the orientation bias trends in  $\sigma_4$  are somewhat weaker for shallower  $\gamma_{\text{dm}} = 0.5$  models, and stronger for steeper  $\gamma_{\text{dm}} = 1.5$  models, at the level of 10 to 30 per cent; whereas for  $\sigma_2$  the degree of orientation bias is roughly the same for  $\gamma_{\text{dm}} = 0.5$  and for  $\gamma_{\text{dm}} = 1.5$ . This may occur because using a shallower  $\gamma_{\text{dm}}$  makes the rounder stellar component more significant for the lensing properties, decreasing the overall flattening and hence decreasing the four-image cross-section.

### 3.2 Shape

Next we study *orientation-averaged* lensing cross-sections to see whether there are significant biases related to the intrinsic shape of the galaxy. Unless explicitly noted, we again use our fiducial cusped models with  $\gamma_{\text{dm}} = 1$ . Table 2 lists the total cross-sections and quad/double ratios of all seven shape models, for each magnification bias mode and for both mass scales. (Note that in some cases, the statistical errors are not identically zero but round to zero at the precision quoted in the table.)

#### 3.2.1 Total cross-section

We first consider how the orientation-averaged unbiased total cross-section varies with model shape for the lower mass model in Table 2. When progressing from spherical to moderately and very oblate shapes,  $\langle\sigma_{\text{tot}}\rangle$  decreases by 8 and 12 per cent, respectively. When progressing from spherical to moderately and very prolate shapes,  $\langle\sigma_{\text{tot}}\rangle$  increases by 6 and 8 per cent, respectively. The triaxial model has  $\langle\sigma_{\text{tot}}\rangle$  that is 3 per cent lower than in the spherical case. Finally, the cross-section for the mixed shape model is the same as that for the moderately oblate model, which suggests that the oblate stellar component is dominant in determining the lensing properties, even in the mixed model. Table 2 shows that these trends are only slightly enhanced for the higher mass model. We conclude that the orientation-averaged unbiased cross-section does *not* depend strongly on the intrinsic model shape, even for significant changes in shape. In other words, while there is an orientation bias such that non-spherical lens galaxies are more likely to be aligned along the line-of-sight, there is no shape bias that would make non-spherical galaxies significantly over- or under-abundant in strong lens samples.

Once we include magnification bias, the trends with model shape tend to be somewhat stronger, particularly when the survey flux limit is in the bright (steep) part of the luminosity function. However, even in the worst case, the variations in  $\langle\sigma_{\text{tot}}\rangle$  with model shape are a maximum of  $\sim 30$  per cent, rather than  $\sim 10$  per cent in the unbiased case. This is clearly not a selection bias that will drastically alter the distribution of model shapes for strong lensing systems from the distribution of model shapes for all galaxies at that mass. Furthermore, while we have only tested specific sets of intrinsic axis ratios for the non-spherical shapes, the similarity of the cross-sections to the spherical case suggests that at least for axis ratios  $b/a$  and  $c/a$  equal to or greater than the cases we have tested, our conclusions still apply.

With Table 2 we can consider how the shape of the

galaxy affects the mass bias (at least for  $\gamma_{\text{dm}} = 1$ ; recall that Section 2.4 shows how the mass bias depends on  $\gamma_{\text{dm}}$  for spherical models). For all model shapes, the unbiased total cross-section increases by a factor of  $\sim 3$  from the lower to the higher mass scale. The difference is even larger when considering biased cross-sections, up to a factor of  $\sim 9$  for cases with a flux limit in the steepest part of the luminosity function. We infer that mass bias is not very sensitive to galaxy shape (which is not surprising given that there is little dependence of  $\langle\sigma_{\text{tot}}\rangle$  on shape). However, mass bias is sensitive to magnification bias such that in surveys with flux limits on the steeper part of the quasar luminosity function, the observed strong lensing systems will be preferentially skewed towards higher masses even more so than for those surveys with fainter flux limits.

Our results compare well with those in the literature. Keeton & Kochanek (1998) noted that there is a significant orientation bias for strong lensing by spiral galaxies, but found that the orientation-averaged cross-sections of disk+halo models differ from those of spherical models by  $\lesssim 10$  per cent. Huterer et al. (2005)<sup>3</sup> used single-component projected isothermal ellipsoid models and found that, when the Einstein radius is fixed, the ellipticity affects lensing cross-sections at the few per cent level. One instance of a shape bias was found by Oguri & Keeton (2004), who found that  $\langle\sigma_{\text{tot}}\rangle$  increases with triaxiality for massive, generalised NFW halos. However, they noted that the increase was driven by the cross-section for three-image lenses—an effect that was enhanced by the use of a single-component generalised NFW dark matter halo without a stellar component, such that the inner density profile was relatively shallow and hence quite prone to create three-image lens systems. Such models may or may not be reasonable for the massive halos of galaxy clusters, but are certainly not realistic models for galaxies. Even so, it is interesting to note that Oguri & Keeton (2004) found the net cross-section for two- and four-image lenses to be roughly independent of halo shape. Altogether, we conclude that there is general consensus that shape bias is not a strong effect in strong lensing by galaxies.

Finally, we note that our conclusions about shape bias are not a strong function of mass model parameters such as  $\gamma_{\text{dm}}$ . This conclusion is expected given our agreement with other papers that use quite different mass models. However, as in Section 2.4 and here, our conclusion regarding the degree of mass-based selection bias does depend on  $\gamma_{\text{dm}}$  and the magnification bias mode.

#### 3.2.2 Quad/double ratio

Next, we consider the ratio of the orientation-averaged four-image and two-image cross-sections to understand the relative abundances of quad and double lenses. Table 2 lists

<sup>3</sup> Kochanek (1996), Keeton et al. (1997), Rusin & Tegmark (2001), and Chae (2003) also computed lensing cross-sections for isothermal ellipsoid lens models with different ellipticities, but those studies did not isolate and discuss the effects of shape on the total cross-section in the same way that Huterer et al. (2005) did.

**Table 2.** Lensing cross-sections averaged over all orientations, for each model shape and magnification bias mode, for the fiducial dark matter concentration and inner slope  $\gamma_{\text{dm}} = 1$ , and for both mass scales.

Shape	Bias mode	Lower mass		Higher mass	
		$\langle\sigma_{\text{tot}}\rangle$ (arcsec <sup>2</sup> )	$\langle\sigma_4\rangle/\langle\sigma_2\rangle$	$\langle\sigma_{\text{tot}}\rangle$ (arcsec <sup>2</sup> )	$\langle\sigma_4\rangle/\langle\sigma_2\rangle$
Spherical	Unbiased	0.53 ± 0.00	0.000 ± 0.000	1.63 ± 0.00	0.000 ± 0.000
	Faintest, total	1.08 ± 0.00	0.000 ± 0.000	4.18 ± 0.01	0.000 ± 0.000
	Faintest, second	0.72 ± 0.00	0.000 ± 0.000	2.97 ± 0.01	0.000 ± 0.000
	Medium, total	1.97 ± 0.01	0.000 ± 0.000	8.34 ± 0.02	0.000 ± 0.000
	Medium, second	1.02 ± 0.01	0.000 ± 0.000	5.09 ± 0.02	0.000 ± 0.000
	Brightest, total	25.12 ± 0.22	0.000 ± 0.000	163.52 ± 0.85	0.000 ± 0.000
	Brightest, second	5.78 ± 0.10	0.000 ± 0.000	51.56 ± 0.56	0.000 ± 0.000
Moderately oblate	Unbiased	0.49 ± 0.00	0.054 ± 0.001	1.46 ± 0.01	0.264 ± 0.004
	Faintest, total	0.98 ± 0.00	0.089 ± 0.001	3.65 ± 0.02	0.366 ± 0.005
	Faintest, second	0.64 ± 0.00	0.093 ± 0.001	2.47 ± 0.01	0.362 ± 0.005
	Medium, total	1.77 ± 0.01	0.107 ± 0.002	7.21 ± 0.04	0.406 ± 0.006
	Medium, second	0.87 ± 0.00	0.132 ± 0.002	4.08 ± 0.02	0.429 ± 0.006
	Brightest, total	22.09 ± 0.09	0.251 ± 0.004	138.28 ± 0.78	0.645 ± 0.009
	Brightest, second	4.01 ± 0.02	0.611 ± 0.009	36.16 ± 0.23	1.055 ± 0.013
Very oblate	Unbiased	0.47 ± 0.00	0.110 ± 0.002	1.48 ± 0.01	0.540 ± 0.010
	Faintest, total	0.93 ± 0.00	0.168 ± 0.002	3.73 ± 0.03	0.684 ± 0.012
	Faintest, second	0.60 ± 0.00	0.173 ± 0.002	2.51 ± 0.02	0.662 ± 0.011
	Medium, total	1.66 ± 0.01	0.198 ± 0.003	7.38 ± 0.06	0.742 ± 0.013
	Medium, second	0.81 ± 0.00	0.239 ± 0.003	4.15 ± 0.03	0.750 ± 0.012
	Brightest, total	20.64 ± 0.10	0.448 ± 0.006	143.55 ± 1.14	1.077 ± 0.017
	Brightest, second	3.90 ± 0.03	0.957 ± 0.013	37.46 ± 0.33	1.465 ± 0.021
Moderately prolate	Unbiased	0.56 ± 0.00	0.010 ± 0.000	1.77 ± 0.00	0.035 ± 0.001
	Faintest, total	1.14 ± 0.00	0.020 ± 0.000	4.49 ± 0.01	0.057 ± 0.001
	Faintest, second	0.74 ± 0.00	0.021 ± 0.000	3.07 ± 0.01	0.058 ± 0.001
	Medium, total	2.06 ± 0.00	0.025 ± 0.001	8.92 ± 0.02	0.065 ± 0.001
	Medium, second	1.01 ± 0.00	0.032 ± 0.001	3.07 ± 0.01	0.058 ± 0.001
	Brightest, total	25.61 ± 0.09	0.064 ± 0.001	172.87 ± 0.56	0.109 ± 0.002
	Brightest, second	4.78 ± 0.03	0.166 ± 0.003	45.60 ± 0.23	0.203 ± 0.003
Very prolate	Unbiased	0.57 ± 0.00	0.022 ± 0.000	1.83 ± 0.01	0.078 ± 0.001
	Faintest, total	1.15 ± 0.00	0.040 ± 0.001	4.60 ± 0.01	0.117 ± 0.002
	Faintest, second	0.74 ± 0.00	0.042 ± 0.001	3.13 ± 0.01	0.117 ± 0.002
	Medium, total	2.07 ± 0.01	0.049 ± 0.001	9.11 ± 0.03	0.131 ± 0.002
	Medium, second	1.00 ± 0.00	0.062 ± 0.001	5.19 ± 0.02	0.142 ± 0.002
	Brightest, total	25.51 ± 0.10	0.119 ± 0.002	174.92 ± 0.64	0.210 ± 0.003
	Brightest, second	4.59 ± 0.03	0.304 ± 0.006	45.29 ± 0.25	0.370 ± 0.005
Triaxial	Unbiased	0.51 ± 0.00	0.042 ± 0.000	1.55 ± 0.00	0.176 ± 0.002
	Faintest, total	1.03 ± 0.00	0.073 ± 0.001	3.86 ± 0.01	0.260 ± 0.002
	Faintest, second	0.66 ± 0.00	0.077 ± 0.001	2.60 ± 0.01	0.261 ± 0.002
	Medium, total	1.86 ± 0.00	0.089 ± 0.001	7.62 ± 0.02	0.292 ± 0.002
	Medium, second	0.90 ± 0.00	0.113 ± 0.001	4.27 ± 0.01	0.321 ± 0.003
	Brightest, total	23.07 ± 0.06	0.218 ± 0.002	144.19 ± 0.44	0.490 ± 0.004
	Brightest, second	3.96 ± 0.02	0.636 ± 0.006	35.99 ± 0.14	0.983 ± 0.007
Mixed	Unbiased	0.49 ± 0.00	0.059 ± 0.001	1.47 ± 0.00	0.220 ± 0.002
	Faintest, total	0.98 ± 0.00	0.099 ± 0.001	3.69 ± 0.01	0.316 ± 0.003
	Faintest, second	0.63 ± 0.00	0.103 ± 0.001	2.49 ± 0.01	0.317 ± 0.003
	Medium, total	1.77 ± 0.00	0.118 ± 0.001	7.28 ± 0.02	0.354 ± 0.003
	Medium, second	0.86 ± 0.00	0.148 ± 0.001	4.10 ± 0.01	0.385 ± 0.003
	Brightest, total	22.24 ± 0.06	0.281 ± 0.003	139.49 ± 0.46	0.582 ± 0.005
	Brightest, second	3.94 ± 0.02	0.752 ± 0.007	35.64 ± 0.14	1.103 ± 0.008

$\langle\sigma_4\rangle/\langle\sigma_2\rangle$  for all shape models, for both mass scales. Naturally, in the spherical case this ratio is identically zero. For oblate models, the abundance of four-image lens systems can be quite significant, particularly when the flux limit is in the steep part of the luminosity function: for example, for

the very oblate, higher mass model the quad/double ratio ranges from  $\sim 0.5$  in the unbiased case to  $\sim 1.5$  for some of the magnification bias modes. Prolate systems, in contrast, have fairly low quad/double ratios, reaching a maximum of 37 per cent. The trend with model shape is sensi-

ble: for the moderately and very oblate cases the smallest axis ratio  $(c/a)_{\text{dm}}$  is (respectively) 0.50 and 0.36, whereas in the moderately and very prolate case the smallest axis ratio  $(b/a)_{\text{dm}} = (c/a)_{\text{dm}}$  is (respectively) 0.71 and 0.60. Thus, the maximum projected ellipticity is lower in the prolate case, so there are fewer four-image lenses.

The trend with magnification bias is due to the fact that four-image systems have preferentially higher magnifications than two-image systems. Moreover, four-image lenses often have two or more particularly bright images, which is why the quad/double ratio is especially high if we compute magnification bias using the second-brightest image (see also Fig. 1). In the triaxial case, the quad/double ratio is particularly dependent on how magnification bias is treated, ranging from 0.04 to 1.00.

Generically, for a given shape model we find that  $\langle\sigma_4\rangle/\langle\sigma_2\rangle$  is larger for our higher mass model, because at the higher mass scale the dark matter component (which is flatter than the stellar component) plays a more important role. Our conclusion is seemingly at odds with that of Möller et al. (2007), who found that the four-image systems in their simulations are preferentially at lower velocity dispersion than the two-image systems. However, Möller et al. (2007) also found that the four-image systems have lens galaxies with a more pronounced disk component, in which case the appropriate comparison is not at fixed DM halo shape. Thus, there is no real disparity between our results and theirs, since we find that oblateness (as would occur with a pronounced disk component) strongly increases  $\langle\sigma_4\rangle/\langle\sigma_2\rangle$ .

Our results are compatible with the conventional wisdom that the quad/double ratio in strong lensing offers a valuable probe of the density shapes in the inner regions of galaxies (e.g., Rusin & Tegmark 2001; Oguri 2007). But magnification bias also plays a very important role (see also Huterer et al. 2005; Möller et al. 2007). In particular, Oguri (2007) suggests that magnification bias may explain why there is a higher fraction of four-image lenses in radio surveys than in optical surveys. He suggests that the source luminosity function is steeper in radio surveys than in optical surveys (at least, in optical surveys that probe deeper than the break in the quasar luminosity function), which enhances magnification bias and (as we have seen) increases the quad/double ratio in radio surveys.

### 3.2.3 Three-image cross-section

The final shape-related question we address is which shapes give rise to three-image lens systems. They can only occur in cases of such high projected ellipticity that the tangential caustic protrudes beyond the radial caustic. For the lower-mass model, we find three-image systems only for the very oblate model, with a cross-section that depends sensitively on the dark matter inner slope. This dependence may arise from the fact that our dark matter is flatter than the stellar components, and models with steeper dark matter inner slope are more dark matter-dominated in the region where strong-lensing is important. Thus, for example, the three-image cross-section (unbiased) for this very oblate lower mass model averages to zero for  $\gamma_{\text{dm}} = 0.5$  and  $\gamma_{\text{dm}} = 1$ , and is small but non-zero for  $\gamma_{\text{dm}} = 1.5$  (but  $\langle\sigma_3\rangle$  is still just 0.3 per cent of  $\langle\sigma_{\text{tot}}\rangle$ ). Magnification bias can enhance

the relative abundance of three-image systems by up to a factor of  $\sim 10$  depending on the survey flux limit (with the greatest enhancement when the flux limit is on the bright end). Naturally these systems can only occur in the oblate case when the galaxy is seen close to edge-on, which is a fairly extreme orientation-related selection bias inherent to such systems.

For the higher-mass model, three-image lens systems occur for both the moderately and very oblate cases (presumably because the higher-mass model is inherently more dark matter-dominated and therefore flatter); and there is again a strong trend with  $\gamma_{\text{dm}}$ . For the very oblate shape, the unbiased three-image lens system abundance ( $\langle\sigma_3\rangle/\langle\sigma_{\text{tot}}\rangle$ ) ranges from 0.7 to 8 per cent as  $\gamma_{\text{dm}}$  changes from 0.5 to 1.5, a factor of 10 increase. For the most extreme magnification bias mode ( $4L_*$  with the total magnification), the increase is from  $\sim 3$  per cent at  $\gamma_{\text{dm}} = 0.5$  to  $\sim 20$  per cent at  $\gamma_{\text{dm}} = 1.5$  (a factor of 7). An observational scarcity of three-image lens systems with group-mass lenses can therefore constrain the abundance of strongly oblate matter distributions (but see below). For this mass scale, the triaxial and mixed models also give rise to three-image lenses, but with a relative abundance that is below 1 per cent for all  $\gamma_{\text{dm}}$  and magnification bias modes.

We contrast this result with the findings in Oguri & Keeton (2004), who use single-component generalised NFW profiles with an axis ratio distribution (rather than fixed shapes as used here) to study the trends of  $\langle\sigma_3\rangle/\langle\sigma_{\text{tot}}\rangle$  with  $\gamma_{\text{dm}}$ . That work suggests that the three-image abundance increases as  $\gamma_{\text{dm}}$  gets *shallower*, which seems to contradict our trend. The difference between these two results stems from a difference in modeling assumptions: in their case, without a fixed stellar component creating a lower bound to the central density, decreasing  $\gamma_{\text{dm}}$  strongly affects the (lens-plane) inner critical curve (which is very sensitive to the central slope of the density profile), shrinking the (source-plane) radial caustic. However, the tangential caustic does not shrink as much, because it depends primarily on the projected ellipticity. As a result, decreasing  $\gamma_{\text{dm}}$  actually increases the area that is inside the tangential caustic and outside the radial one, where three-image systems originate. In contrast, when we decrease  $\gamma_{\text{dm}}$  the radial caustic does not shrink very much, since we have a fixed stellar component. However, the stellar component becomes much more dominant, and since we have modeled it as being rounder, this means the tangential caustic will shrink. The result is that the area inside the tangential caustic and outside the radial one, and therefore the three-image lensing system abundance, is reduced.

This comparison suggests that the predicted abundance of three-image strong lenses is quite dependent on modeling assumptions, particularly on the ratio of stellar to dark matter mass and the assumed shapes for the two components. Another potential concern in studying the statistics of three-image lenses is that a four-image lens could be misclassified as a three-image system if one of the images is too faint to be detected. Since typically  $\langle\sigma_4\rangle \gg \langle\sigma_3\rangle$ , any small rate of contamination from misclassified four-image lenses could corrupt the three-image sample. In practice, the frequency with which such errors may occur will depend sensitively on the galaxy model and on the survey parameters, so a detailed

exploration is beyond the scope of this paper. For now, we conclude that the abundance of three-image lenses contains interesting information about the abundance of very oblate galaxies, but there may be practical challenges in extracting that information from observed lens samples.

### 3.3 Magnification bias

As an aside, we now investigate whether the conversion from unbiased to the various biased cross-sections can be quantified with a single number for each magnification bias mode, independent of mass, shape, dark matter inner slope, or the number of images. This would allow considerable simplification, not only in the presentation of our results, but also in future calculations. We again refer to the orientation-averaged cross-sections in Table 2.

First, we find that for  $\gamma_{\text{dm}} = 1$  (as in the table), and for a given mass scale, the conversion from unbiased to biased  $\sigma_{\text{tot}}$  is relatively independent of shape. This statement is true within  $\sim 2$  per cent for the fainter flux limits, or within  $\lesssim 10$  per cent for the brightest flux limit. However, the conversion does depend strongly on  $\gamma_{\text{dm}}$  and mass. In retrospect, this is relatively easy to understand, because the biased cross-section depends not just on the lensing caustics, but also on the lensing magnification as a function of position, which in turn depends on how the projected density is distributed within the Einstein radius. Changing the dark matter inner slope changes both the caustics and the magnification distribution, and not necessarily in the same way. Likewise, the different mass scales have different balances of stellar and dark matter components, each with its own density profile, so the conversion from unbiased to biased cross-sections is not the same for our lower and higher mass scales.

Furthermore, because the four-image cross-section depends on the projected shape (Section 3.2), the conversion of the quad/double ratio from the unbiased to the biased cases depends not just on  $\gamma_{\text{dm}}$  and the mass, but also on the shape. We therefore conclude that for the mass models used here, there is no simple conversion from unbiased to biased cross-sections that would allow us to simplify the presentation of our results. Selection biases in  $\sigma_{\text{tot}}$  and  $\sigma_4/\sigma_2$  with the form of the mass density profile may depend strongly on the survey detection strategy and flux limit. Consequently, we continue to present results for the different magnification bias modes throughout the rest of this paper.

## 4 INNER SLOPE

We now examine the role of the galaxy density profile in more detail. We study how the dark matter inner slope  $\gamma_{\text{dm}}$  affects orientation-averaged cross-sections (Section 4.1) as well as lens image separation distributions (Section 4.2). In Section 4.3 we extend the discussion of profile-dependent selection biases to consider the effect of adiabatic contraction on the strong lensing cross-section (for spherical models only).

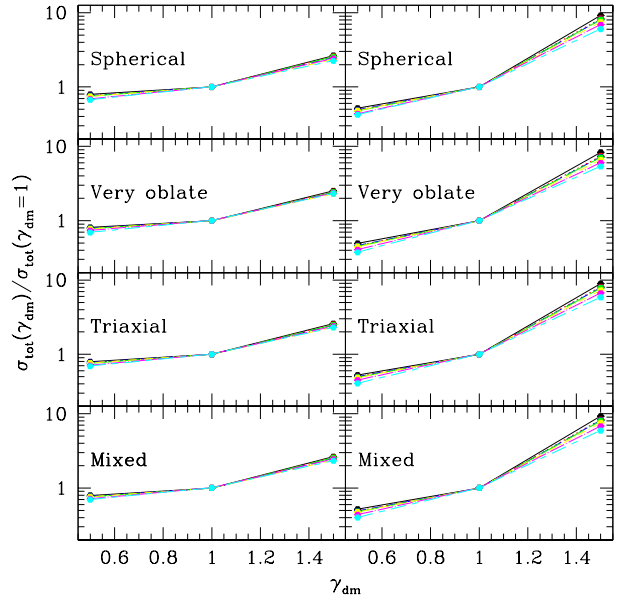


**Figure 3.** Variation of total, orientation-averaged lensing cross-section with  $\gamma_{\text{dm}}$  for the lower (left) and higher (right) mass scales for different shape models as labeled on the plot, with the magnification bias mode indicated as in Fig. 1.

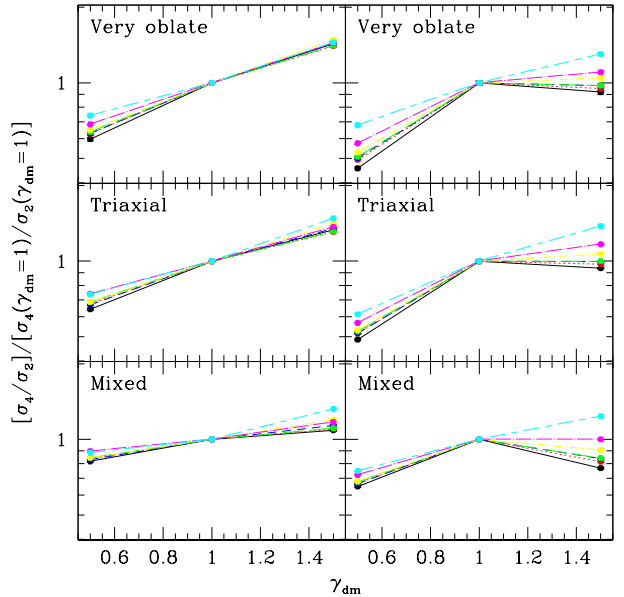


**Figure 4.** Variation of the orientation-averaged quad/double ratio with  $\gamma_{\text{dm}}$  for the lower (left) and higher (right) mass scales for different shape models as labeled on the plot, with magnification bias mode indicated as in Fig. 1.

### 4.1 Inner slope

In the sections that follow, we typically use orientation-averaged cross-sections. While in sections that dealt with orientation and halo shape, we have introduced the notation  $\langle \sigma_{\text{tot}} \rangle$  to highlight the difference between cross-sections for a single orientation versus orientation-averaged cross-sections,

we now revert to simply using  $\sigma_{\text{tot}}$  for orientation-averaged cross-sections since they are now our sole focus.

Fig. 3 shows the variation of the total cross-section with the dark matter inner slope  $\gamma_{\text{dm}}$  for both mass scales, for four of the seven shapes and all seven magnification bias modes. In order to highlight the variation with  $\gamma_{\text{dm}}$  (and to fit all results for a given shape in a single panel), we normalise  $\sigma_{\text{tot}}$  for each magnification bias mode by the corresponding values when  $\gamma_{\text{dm}} = 1$  (given in Table 2). Statistical error bars are shown on the plot, but they are generally smaller than the sizes of the points themselves due to the large number of Monte Carlo realisations. Fig. 4 shows analogous results for the quad/double ratios (once again, normalised by the values at  $\gamma_{\text{dm}} = 1$  given in Table 2). We again show different shape models, although we eliminate the spherical model since its four-image cross-section is identically zero.

The total lensing cross-section for the lower mass model (Fig. 3, left column) shows several interesting trends with  $\gamma_{\text{dm}}$ . First, as we expect,  $\sigma_{\text{tot}}$  increases with  $\gamma_{\text{dm}}$  because the projected mass density is higher in the inner parts for steeper  $\gamma_{\text{dm}}$ . Second, all the curves for a given mass scale are nearly the same, with  $\sigma_{\text{tot}}$  decreasing by 20 to 30 per cent when going from  $\gamma_{\text{dm}} = 1$  to  $\gamma_{\text{dm}} = 0.5$ , and increasing by a factor of  $\sim 3$  when going from  $\gamma_{\text{dm}} = 1$  to  $\gamma_{\text{dm}} = 1.5$ . The variation within the quoted ranges depends only slightly on the magnification bias mode, and is nearly independent of the shapes considered here. For the higher mass scale (Fig. 3, right column), we likewise see that the results are consistent for different shapes. At this mass scale,  $\sigma_{\text{tot}}$  decreases by 50–70 per cent going from  $\gamma_{\text{dm}} = 1$  to  $\gamma_{\text{dm}} = 0.5$ , and it increases by factors of 6–10 going from  $\gamma_{\text{dm}} = 1$  to  $\gamma_{\text{dm}} = 1.5$  (where the quoted range encompasses the different magnification bias modes). The reason the dark matter inner slope causes more significant selection bias for the higher mass model is that the flatter dark matter is more prominent in that model.

To understand the strong variation with  $\gamma_{\text{dm}}$  further, we explore a finer grid in  $\gamma_{\text{dm}}$  in Section 5.1 below, and we compare the variation in the cross-section with the variation in the projected dark matter fraction. However, it is apparent from paper I figure 6 that the projected mass density (and therefore the lensing properties) is dominated on small scales by the stellar component for  $\gamma_{\text{dm}} = 0.5$  and  $\gamma_{\text{dm}} = 1$ , whereas the dark matter component has a significant contribution everywhere for  $\gamma_{\text{dm}} = 1.5$ . Consequently, the cross-section variation is quite likely related to the change in the projected dark matter fraction.

Next, we consider the quad/double ratio for the lower mass model in the left column of Fig. 4. For all shapes shown here, this ratio is roughly exponential in  $\gamma_{\text{dm}}$ ,  $\sigma_4/\sigma_2 \propto \exp(0.85\gamma_{\text{dm}})$ , once again roughly independent of model shape and with consistent trends for all magnification bias modes. Moving to the higher mass scale in the right column, we see rather different results: the quad/double ratio increases from  $\gamma_{\text{dm}} = 0.5$  to  $\gamma_{\text{dm}} = 1$ , but then approximately flattens out from  $\gamma_{\text{dm}} = 1$  to  $\gamma_{\text{dm}} = 1.5$ . There is actually a slight decrease in  $\sigma_4/\sigma_2$  for the unbiased cross-section, and a slight increase for the significant magnification bias modes. This result involves a combination of several effects, the sizes of which approximately cancel, and which are complicated by the fact that we are working with orientation-averaged quantities. First, examination of the mock lens systems sug-

gests that the radial caustic moves strongly outwards for  $\gamma_{\text{dm}} = 1.5$  for the higher mass scale (leading to the very large increase in  $\sigma_{\text{tot}}$  shown in Fig. 3). The tangential caustic increases in size somewhat, because it depends predominantly on the projected shape (which is flatter at high  $\gamma_{\text{dm}}$  due to the dominant DM component), so while  $\sigma_4$  increases, so does  $\sigma_2 \approx \sigma_{\text{tot}} - \sigma_4$ , thus leading to a flattening out of  $\sigma_4/\sigma_2$ . Because the increase in  $\sigma_{\text{tot}}$  is not nearly as much for the lower mass model when going from  $\gamma_{\text{dm}} = 1$  to 1.5 (due to the lower dark matter fraction),  $\sigma_4/\sigma_2$  does not level out as for the higher mass model. The trend with magnification bias is also understandable: for more significant magnification bias (higher flux limit and steeper luminosity function), the inner regions where 4-image systems dominate become more important, which is why for the higher mass model the biased  $\sigma_4/\sigma_2$  can still increase slightly when going from  $\gamma_{\text{dm}} = 1$  to 1.5 even though the unbiased quad ratio decreases.

Several previous studies (e.g., Porciani & Madau 2000; Keeton & Madau 2001; Wyithe et al. 2001; Li & Ostriker 2002; Huterer & Ma 2004) used spherical single-component mass models to examine how the lensing cross-section depends on the inner slope of the density profile. Keeton & Madau (2001) found in particular that the cross-section variation could be explained mainly by changes in the fraction of the total mass that lies within some fiducial radius. The simple scaling with the “core mass fraction” is probably broken in our models by the presence of the stellar component, although we do examine whether there is some analogous scaling in Section 5.1 below. There is general consensus that the total cross-section can increase fairly dramatically as the inner density profile steepens, although we believe our two-component models better isolate the effects of the dark matter slope alone.

In conclusion, there is a strong selection bias in the total cross-section with  $\gamma_{\text{dm}}$  that can amount to factors of a few (particularly within the upper end of the allowed range); and this bias is remarkably insensitive to the model shape and only mildly sensitive to the magnification bias (survey flux limit and detection strategy). The selection bias with  $\gamma_{\text{dm}}$  in the quad/double ratio can amount to several tens of per cent, and is likewise relatively insensitive to the model shape and magnification bias mode.

In this section, we have focused on quantities averaged over orientation. In Appendix A, we indicate how the variation of cross-section with  $\gamma_{\text{dm}}$  depends only mildly on orientation. This result is relevant only when a special subset of strong lenses are selected based on their projected shape.

## 4.2 Image separation distributions

We next consider the effects of the dark matter inner slope  $\gamma_{\text{dm}}$  on the image separation distribution, and consider whether this is a magnification bias-dependent quantity. This calculation is done separately in the spherical and the non-spherical cases.

### 4.2.1 Spherical models

We begin with cusped, spherical density profile models, which lead only to strong lensing systems with two images. We first consider what to expect for the image separation

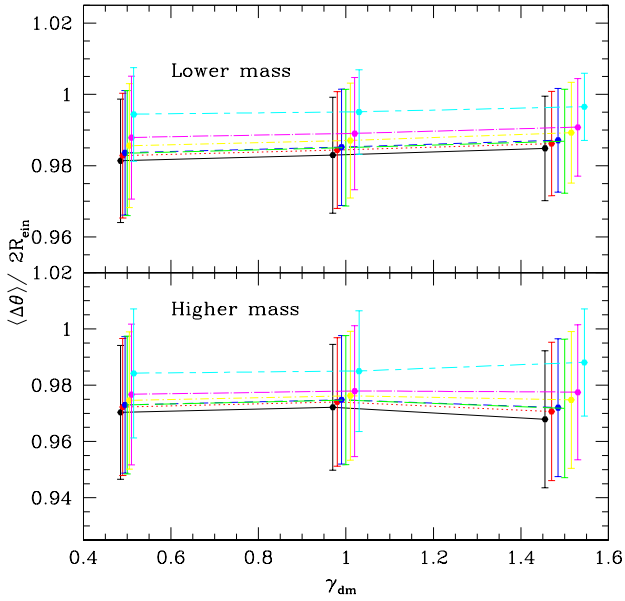


**Figure 5.** Mean (points) and width (errorbars) of the image separation distribution for the spherical shape model, in units of  $2R_{\text{ein}}$ , as a function of  $\gamma_{\text{dm}}$ . Points are horizontally offset for clarity, but all measurements are with the values of  $\gamma_{\text{dm}} = \{0.5, 1, 1.5\}$ . Line colours and types indicate the magnification bias mode, as described in the caption for Fig. 1.

distribution based on general considerations. By definition, the Einstein radius  $R_{\text{ein}}$  for a circularly-symmetric projected mass distribution is the radius at which the lensed image is a ring because the source is located precisely behind the lens. In that case, the image separation is  $\Delta\theta = 2R_{\text{ein}}$ . Consequently, we expect that regardless of the form of the density profile, it must approach  $2R_{\text{ein}}$ , because the sources near the source plane origin produce precisely that image separation.

The simplest comparison we can make is against the very simple image separation distribution for the SIS density profile, which is a delta function at  $2R_{\text{ein}}$ :

$$p_{\text{SIS}}(\Delta\theta) = \delta(\Delta\theta - 2R_{\text{ein}}). \quad (5)$$

We ask, then, how the complexity of our mass models causes the image separation distribution to deviate from this simple form.

Fig. 5 shows the mean image separation in units of twice the Einstein radius as a function of  $\gamma_{\text{dm}}$ , for all magnification bias modes. The standard deviation of the image separation distribution is shown as an errorbar. There are a few conclusions we can draw from this plot. First, the image separation distribution depends on  $\gamma_{\text{dm}}$  almost exclusively through its dependence on  $R_{\text{ein}}$ . Second, despite the complexity of the mass models, to lowest order the distributions are remarkably close to the distributions for a pure SIS, very narrow and with an average that is only  $\sim 2$ – $3$  per cent below  $2R_{\text{ein}}$ . Finally, there is a minor (for practical purposes) but nonzero dependence on the magnification bias mode. The mean of the image separation distribution increases with more significant magnification bias, approaching  $2R_{\text{ein}}$  from below, because the magnification is highest for a source near the origin, where  $\Delta\theta$  is precisely  $2R_{\text{ein}}$ .

We have quantified the image separation statistics using the usual mean and standard deviation. However, the distributions  $p(\Delta\theta)$  are not remotely Gaussian or even peaked at  $\langle \Delta\theta \rangle$ ; rather, they are steeply increasing functions of  $\Delta\theta$  that are truncated abruptly at  $\Delta\theta = 2R_{\text{ein}}$ . We use the deflection angle profile  $\alpha(R')$  in paper I figure 7 to explain the shape of this distribution, and why the mean is so close to the SIS result. As shown there, for the three cusped models,  $\alpha(\theta)$  is nearly flat and equal to  $R_{\text{ein}}$  from  $R' \sim R_{\text{ein}}/4$  until well above  $R_{\text{ein}}$ . Consequently, the image separations should be below  $2R_{\text{ein}}$  for those small subset of images that appear to be near the origin in the lens plane, but approach  $2R_{\text{ein}}$  for the majority of the images.

Our results are consistent with those of Oguri et al. (2002), who study image separations for spherical, single-component, generalised NFW models, and also find that it is close to, but slightly below,  $2R_{\text{ein}}$ . In light of that result, ours is not surprising, since the superposition of a stellar component with a generalised NFW model tends to yield a composite model that is closer to isothermal near  $R_{\text{ein}}$  and therefore more likely to give quasi-isothermal image separation distributions.

Thus, for spherical models, the changes in the image separation distribution due to changes in density profile parameters (mass,  $\gamma_{\text{dm}}$ ) arise almost exclusively through the change in the Einstein radius. This is a remarkably simple result given the complexity of the mass models used. We note, however, that while the physical scaling of the image separation distribution is simple, there may be observational selection biases due to resolution limits (more likely to miss lenses with smaller  $R_{\text{ein}}$ ) or due to finite apertures for the image search (more likely to miss lenses with larger  $R_{\text{ein}}$ ). To estimate the effects of selection bias in any given survey, it will be necessary to supplement the physical selection effects we study here with an analysis of observational selection effects.

#### 4.2.2 Non-spherical models

For non-spherical models, we have defined the image separation as the maximum separation between any pair of images in a given image system, regardless of the total number of images. We have then calculated the mean and width of the image separation distribution as a function of  $\gamma_{\text{dm}}$  for both mass scales, with different extreme configurations in the projected shapes. These results are shown for the unbiased case in Fig. 6, normalised by twice the spherical Einstein radius (i.e., we use the same normalisation factors that went into Fig. 5). As for the spherical case, the effects of magnification bias (not shown) are subtle.

There are a few conclusions we can draw from this plot. First, as expected, the mean of the image separation distribution scales with  $\gamma_{\text{dm}}$  in nearly the same way as the Einstein radius in the spherical case, so the curves are nearly flat. Second, the difference between the means and widths of  $p(\Delta\theta)$  for various shape configurations can be understood simply in terms of the projected shape. For example, for the very oblate and very prolate shapes, the solid lines (edge-on and end-on, respectively) give the highest *mean*  $\Delta\theta$  because they give a larger projected mass density for a given (azimuthally-averaged) separation from the centre of mass than in configurations represented with dashed lines (face-

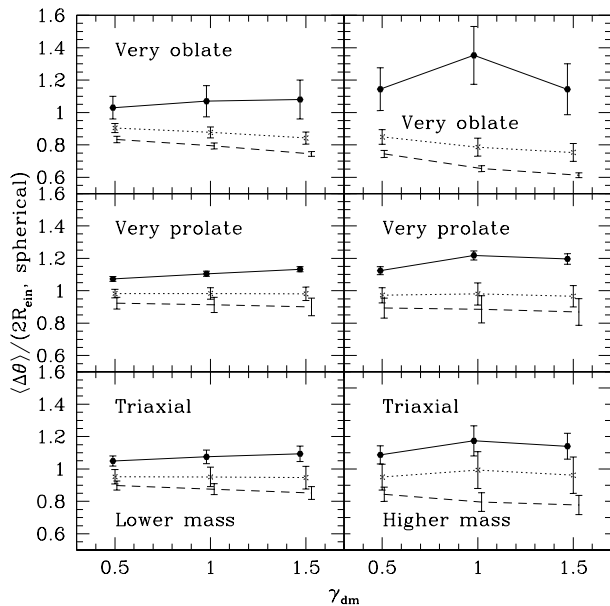


**Figure 6.** Mean (points) and width (errorbars) of the unbiased image separation distribution, relative to  $2R_{\text{ein}}$  for the spherical shape model, as a function of  $\gamma_{\text{dm}}$ . The left and right panels show the lower and higher mass scales, respectively. Points are horizontally offset for clarity, but all measurements are with the values of  $\gamma_{\text{dm}} = \{0.5, 1, 1.5\}$ . The top panels show the very oblate model shape, where the solid line = edge-on, dotted line = intermediate, and dashed line = face-on configuration. The middle panels show the very prolate model shape, where the solid line = end-on, dotted line = intermediate, and dashed line = side-on configuration. The bottom panels show the triaxial model shape, where the solid line = viewed with line-of-sight along  $a$ , dotted line = viewed along  $b$ , and dashed line = viewed along  $c$ .

on and side-on, respectively), consistent with the larger total lensing cross-section. Because the projected ellipticity is higher for the solid line configuration in the oblate case (edge-on) and for the dashed line in the prolate case (side-on), the *width* of the image separation distributions in those cases is larger (depending on where the source is located in the region where lensing occurs, very different image configurations can occur). In the triaxial case, these arguments imply that the mean image separation is highest when viewing along the major axis (solid lines), but the width is highest when viewing along the intermediate axis (dotted lines). When considering the image separation distribution derived from many lenses drawn from galaxies of a given shape with random orientations, we must average the image separation distribution for each orientation weighted by the cross-section  $\sigma_{\text{tot}}$  for that orientation. We have confirmed that the differences between  $\langle \Delta\theta \rangle$  for different orientations relative to the spherical Einstein radius can be accounted for by computing  $R_{\text{ein}}$  from the monopole deflection (equation 26 of Paper I) as  $\alpha_0(R_{\text{ein}}) = R_{\text{ein}}$ .

Our finding that non-spherical models have significantly broader image separation distributions ( $\sim 10$  per cent rather than a few per cent), but mean values that are not strongly different from the spherical case, is consistent with the results in Huterer et al. (2005), who tested this effect using single-component singular isothermal ellipsoid models. The

fact that the image separation distribution is quite close to that for a spherical isothermal model even for these highly non-spherical and non-isothermal models is quite remarkable. The implication is that there may be an observational selection bias that is sensitive to  $\gamma_{\text{dm}}$ , depending on the angular resolution and aperture limits for a particular survey. For example, an inability to find large-separation lens systems would tend to counteract the physical selection bias towards galaxies with steeper dark matter inner slope ( $\gamma_{\text{dm}}$ ), particularly at low redshift.

### 4.3 Adiabatic contraction

As discussed in Paper I, the need for adiabatic contraction of dark matter halos in response to the adiabatic infall of baryons to form a galaxy (Young 1980; Blumenthal et al. 1986; Gnedin et al. 2004; Sellwood & McGaugh 2005) is unclear for early-type galaxies. In this subsection, we test the effects of adiabatic contraction explicitly, for spherical, cusped  $\gamma_{\text{dm}} = 1$  models only. Kochanek & White (2001) previously examined the effect of AC on the strong lensing image separation distribution, and Keeton (2001a) included AC when computing lens statistics, but neither study considered it as a selection bias as we are.

The effects of AC on the projected density profiles are shown in paper I figures 4–7; it increases the dark matter density on scales below  $\sim 10$  kpc. Due to the increased density in the inner regions, we expect an increase in the strong-lensing cross-section. Our purpose is to determine the significance of this increase compared to the increase when changing  $\gamma_{\text{dm}} = 1$  to  $\gamma_{\text{dm}} = 1.5$  without AC.

For the lower mass model, the total lensing cross-section  $\sigma_{\text{tot}}$  increases by a factor of 2.6 when going from  $\gamma_{\text{dm}} = 1$  to  $\gamma_{\text{dm}} = 1.5$ , or slightly less than that for the higher magnification bias modes. In contrast, when going from  $\gamma_{\text{dm}} = 1$  without AC to including AC, the cross-section increases by a factor of  $\sim 2.6$  for the Blumenthal et al. (1986) prescription, or a factor  $\sim 2.0$  for the Gnedin et al. (2004) prescription. These factors are reduced to  $\sim 2.0$  and  $\sim 1.5$  for the higher magnification bias modes.

For the higher mass model, the unbiased  $\sigma_{\text{tot}}$  increases by a factor of 9 when going from  $\gamma_{\text{dm}} = 1$  to  $\gamma_{\text{dm}} = 1.5$ , or as little as 6 for the higher magnification bias modes. In contrast, when going from  $\gamma_{\text{dm}} = 1$  without AC to including AC,  $\sigma_{\text{tot}}$  increases by a factor  $\sim 3.5$  for the original Blumenthal et al. (1986) prescription, or a factor  $\sim 2.3$  for the Gnedin et al. (2004) prescription. These factors are again reduced for the higher magnification bias modes. For comparison, previous studies of the effect of baryonic cooling on strong lensing by *clusters* also found that the cross-section increases by a factor of a few (e.g., Puchwein et al. 2005; Rozo et al. 2006; Wambsganss et al. 2008).

We conclude that AC has typically a less significant effect on the strong lensing cross-section than increasing  $\gamma_{\text{dm}}$  from 1 to 1.5 for both mass scales. Nonetheless, the increases in the strong lensing cross-section due to AC are non-negligible. There are several implications of this finding. First, if AC happens in typically all galaxies of these types (i.e., the assumptions behind it are valid and the changes in profile are preserved through mergers), it suggests that the numbers of strong lenses in upcoming surveys will be significantly higher than predicted given a simple two-component

model that does not include AC. Second, if AC only occurs in massive, early-type galaxies with particular shapes or formation histories, then the ones for which AC does occur are more likely to be strong-lensing systems. Thus, for a given mass system, there may be a selection bias favouring galaxies or groups depending on their formation history.

Improved simulations, better understanding of galaxy formation, and observational results that confirm, contradict, or refine these AC models will be useful for understanding selection biases due to AC. A more detailed exploration is beyond the scope of this paper.

## 5 CONCENTRATION

We now allow more model freedom than in the previous section, varying both the dark matter inner slope  $\gamma_{\text{dm}}$  and the dark matter halo concentration  $c_{\text{dm}}$  on a grid (spherical model only) in Section 5.1. We also consider a more limited set of changes in dark matter halo concentration in the triaxial case in Section 5.2.

### 5.1 Concentration versus inner slope

Here we explore the trade-off between steepening the dark matter inner slope versus increasing the concentration (with fixed stellar component), both of which are expected to increase the lensing cross-section due to the enhanced density of dark matter in the very inner parts of the galaxy.

First, we explore this degeneracy with a relatively fine grid in dark matter inner slope  $\gamma_{\text{dm}}$  and concentration  $c_{\text{dm}}$ , for spherical cusped models only. Our grid has 10 values of  $\gamma_{\text{dm}}$  and 8 values of  $c_{\text{dm}}$  for each mass scale. In accordance with our finding in Section 4.1 that the increase in total cross-section with  $\gamma_{\text{dm}}$  for slopes steeper than unity is extremely rapid at our fiducial concentration, we choose 10 values of  $\gamma_{\text{dm}}$  from 0 to 2, distributed evenly in  $\exp(\gamma_{\text{dm}})$ . To define the grid in concentration, we use the result from  $N$ -body simulations that the distribution of  $c_{\text{dm}}$  values is roughly lognormal around the fiducial concentration, with scatter of 0.15 dex (Bullock et al. 2001). Our 8 values of  $c_{\text{dm}}$  range from  $-3\sigma$  to  $+4\sigma$ , i.e., from  $c_{\text{dm}} = 3.0$  to  $c_{\text{dm}} = 33.4$  for the lower mass scale, and from  $c_{\text{dm}} = 2.0$  to  $c_{\text{dm}} = 22.3$  for the higher mass scale, in steps of  $1\sigma$ . (The grid is skewed towards higher values because of our expectation that the cross-section will get quite large in those cases, a trend we want to track). When we change  $\gamma_{\text{dm}}$  and/or  $c_{\text{dm}}$ , we normalise the profile by fixing  $M_{180}$  and allowing  $\rho_0$  to vary, as discussed in Paper I.

For some of the grid points at high  $\gamma_{\text{dm}}$  and/or  $c_{\text{dm}}$ , the Einstein radius is significantly larger than for our test case (with  $\gamma_{\text{dm}} = 1.5$  and fiducial concentration) that we used to determine adequacy of the box size in Paper I. To avoid box size effects for those grid points we increase the box size by a factor of  $3/2$  (lower mass scale) or 2 (higher mass scale), while maintaining the pixel size. We expect any remaining box size effects to reduce the cross-section for the steepest slopes and highest concentrations, so any trends we see with these parameters could be slightly underestimated. For grid points at lower  $\gamma_{\text{dm}}$  and/or  $c_{\text{dm}}$  than our test case, the Einstein radius is smaller than the  $\gamma_{\text{dm}} = 0.5$ , fiducial concentration case for which we tested resolution. However,

we find that it is at most 15 per cent smaller, because of the unchanging stellar component which means the combined profile cannot get arbitrarily small, and since our resolution choice was conservative in the spherical case, we do not increase the resolution any further.

For each of the 80 grid points, we compute the unbiased and biased lensing cross-sections; since the models are spherical, there is only one cross-section to consider ( $\sigma_{\text{tot}} = \sigma_2$ ,  $\sigma_3 = \sigma_4 = 0$ ). Fig. 7 shows contour plots of the base-10 logarithm of the lensing cross-section for both mass scales. For illustration purposes, we show the unbiased cross-section only, and describe the effects on the biased cross-sections in the text. For the lower mass scale (left panel), the total variation of the unbiased cross-section is a factor of 200; for the higher mass scale (right panel), a factor of 3 200. This difference in dynamic range for the two mass scales is because the higher mass scale was already more dark matter-dominated than the lower mass scale even for  $\gamma_{\text{dm}} = 1$  and the fiducial concentration, so increasing either one or both of those values has a more dramatic effect on the cross-section. Much of this strong variation with cross-section occurs in a fairly small range of  $\gamma_{\text{dm}} \geq 1.3$ , and the very highest cross-sections are only achieved for concentrations that are several  $\sigma$  above the median. Nonetheless, the enormous variation in cross-section across the parameter space suggests that the observed distribution of concentration and inner slopes from strong lensing systems,  $p_{\text{SL}}(\gamma_{\text{dm}}, c_{\text{dm}})$ , may be quite biased compared with the intrinsic distribution (at fixed mass). Indeed, in Section 8.1 below we construct an example to illustrate the bias in the distribution of  $\gamma_{\text{dm}}$  and  $c_{\text{dm}}$  that may be observed in strong lensing surveys. We find that the distribution can be both shifted and broadened by the lensing selection bias. These effects produce a significant (factor of several) enhancement in the abundance of high-concentration halos that, according to the intrinsic distribution, should constitute only  $\sim 1$  per cent of the population.

Next, we look at slices through the grid. For the fiducial concentration itself, the total variation in the cross-section with  $\gamma_{\text{dm}}$  is a factor of 40 (lower mass scale) or nearly 600 (higher mass scale) going from  $\gamma_{\text{dm}} = 0$  to  $\gamma_{\text{dm}} = 2$ . For the fiducial inner slope ( $\gamma_{\text{dm}} = 1$ ), as the concentration varies from  $-3\sigma$  to  $+4\sigma$ , the cross-section varies by a factor of five (lower mass) to several tens (higher mass). Thus, we can conclude that (a) the effects of varying concentration and inner slope of the dark matter are significant, and (b) those effects are (not surprisingly) stronger in systems where the dark matter is more dominant. In either case, it seems clear that efforts to derive the underlying distribution of  $\gamma_{\text{dm}}$  and  $c_{\text{dm}}$  values using strong lensing-selected systems must account for this strong bias in the cross-sections with dark matter inner slope and concentration.

We also find that the trends of the cross-section with  $\gamma_{\text{dm}}$  and  $c_{\text{dm}}$  do not depend too significantly on the magnification bias modes. The total variation across the grid is somewhat smaller for the biased cases than for the unbiased case, because for the steeper slope models the cross-section does not increase as sharply as in the unbiased case.

We further explore the degeneracy between  $\gamma_{\text{dm}}$  and  $c_{\text{dm}}$  by considering, for all models on the grid, the Einstein radius  $R_{\text{ein}}$  and the (projected) dark matter fraction  $f'_{\text{dm}}$  within  $R_{\text{ein}}$ . We expect both to be connected to the lensing cross-section  $\sigma_{\text{tot}}$  in some non-trivial way. Fig. 8 shows the

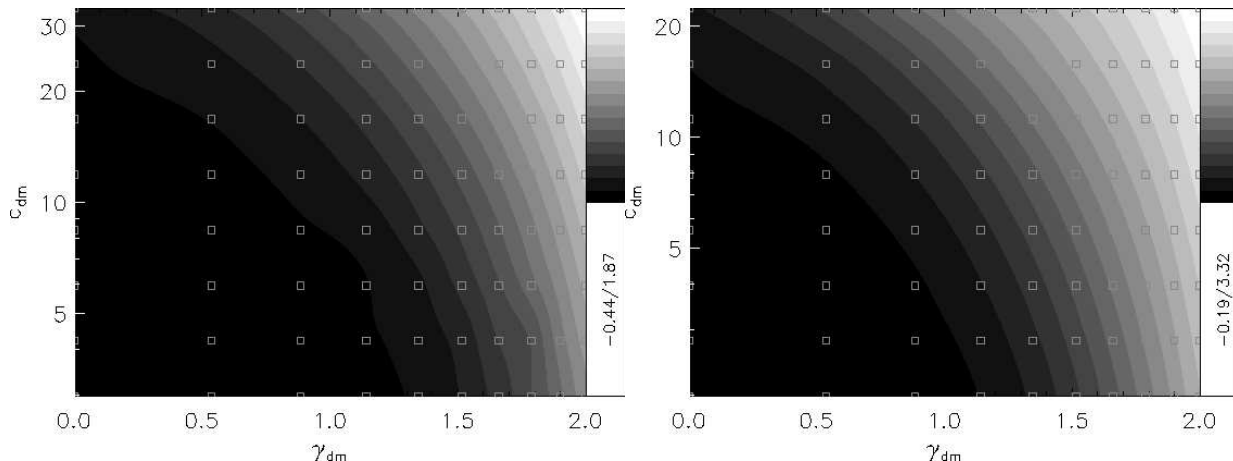


**Figure 7.** Contour plots of the base-10 logarithm of the unbiased cross-section for the lower (left) and higher (right) mass models. Note the different scales for the contour plots. The points on the grid are shown with open squares, with the contours determined via interpolation.

connection between all three quantities for both mass scales (unbiased cross-section only).

First, the relation between the Einstein radius and the dark matter fraction shown in the bottom panels is perfectly one-to-one. This fact follows from our variation of the dark matter profile while fixing the stellar component (see Appendix B for a derivation of this result). Second, the relation between the lensing cross-section and the dark matter fraction, shown in the top panels, is *not* one-to-one, though there clearly is a mean relation with some scatter around it. The Einstein radius is computed in the lens plane, while the cross-section is computed in the source plane. The mapping between the two planes depends on the density profile in a different way than the dark matter fraction depends on the density profile. Therefore, variations in  $c_{\text{dm}}$  and  $\gamma_{\text{dm}}$  affect the mapping, and thus  $\sigma_{\text{tot}}$ , in a different way than they affect  $f'_{\text{dm}}$ , resulting in the observed scatter.

While the mass range under consideration is somewhat different, we can compare our higher mass model qualitatively against the results in Fedeli et al. (2007) for the effect of halo concentration on the strong lensing cross-section. In that paper, they use single-component NFW halos from simulations to model lensing by galaxy clusters (for which this single-component model is not as bad an approximation as it is for galaxy-scale halos, where the baryonic component must be incorporated to obtain even remotely plausible lensing properties). Our results are qualitatively similar to the results in Fedeli et al. (2007), who find that: (a) for a sample with a broad mass range, the lensing cross-section is dominated by those of the highest mass and therefore lowest concentration; and (b) for a sample with a narrow mass range, it is dominated by those clusters at the higher end of the lognormal scatter in halo concentration at fixed mass. Their results are consistent with our finding that the mass increase going from lower to higher mass scale has a far stronger effect on  $\sigma_{\text{tot}}$  than the decrease in concentration, but that at fixed mass, changes in concentration can alter the lensing probabilities by  $\sim 50$  per cent or more. Thus, the abundance of high-concentration halos as lenses should not be taken as a reflection on the underlying distribution of concentrations; and likewise, claims that too many high-concentration

clusters have been observed should be revisited with a concentration distribution from simulations modified by  $\sigma_{\text{tot}}$  as a function of mass and concentration.

We also compare against the results of Kuhlen et al. (2004), who use spherical, single-component NFW model to understand the lensing properties of cluster DM halos. That paper finds results similar to ours: first, that increases in concentration increase  $\sigma_{\text{tot}}$ ; second, that these increases correlate with the mean of the image separation distribution (and therefore  $R_{\text{ein}}$ ), so the distribution of concentration parameters will impact the observed image separation distribution for lensing systems. We can compare our Fig. 15 (lower left) against their fig. 6, which shows the median of the concentration distribution shifting by approximately 70 per cent when accounting for lensing selection bias. Our shift is significantly lower than that (14 per cent) because their analysis uses NFW halos only whereas ours includes a non-negligible stellar component that will tend to reduce the effects of changing the NFW concentration. The different mass range may also play a role in the difference.

These results have implications for the results in Comerford & Natarajan (2007), which includes a compilation of inferred NFW profile concentrations for strong lensing-selected clusters and a fit to a power-law concentration-mass relation. Ignoring issues of possible modeling bias (for example, due to overly simple modeling of cluster shape or substructure), we can attempt to explain the fact that the normalisation of their concentration-mass relation is at least 20 per cent higher than in  $N$ -body simulations. While they consider the possibility that this high normalisation may be due to adiabatic contraction, we note that for our group-scale model (as in Fig. 15) the median of the concentration distribution at fixed halo mass was increased due to selection bias by nearly that amount. There is of course the caveat that their mass range is somewhat higher than ours, but the results of Fedeli et al. (2007) also support this possibility. Consequently, adiabatic contraction (which has not been proven to occur in cluster-mass halos) may not be needed, and selection bias may be significant enough to explain nearly all of this apparent discrepancy with simulations.

## Lower (left) and higher (right) mass spherical models

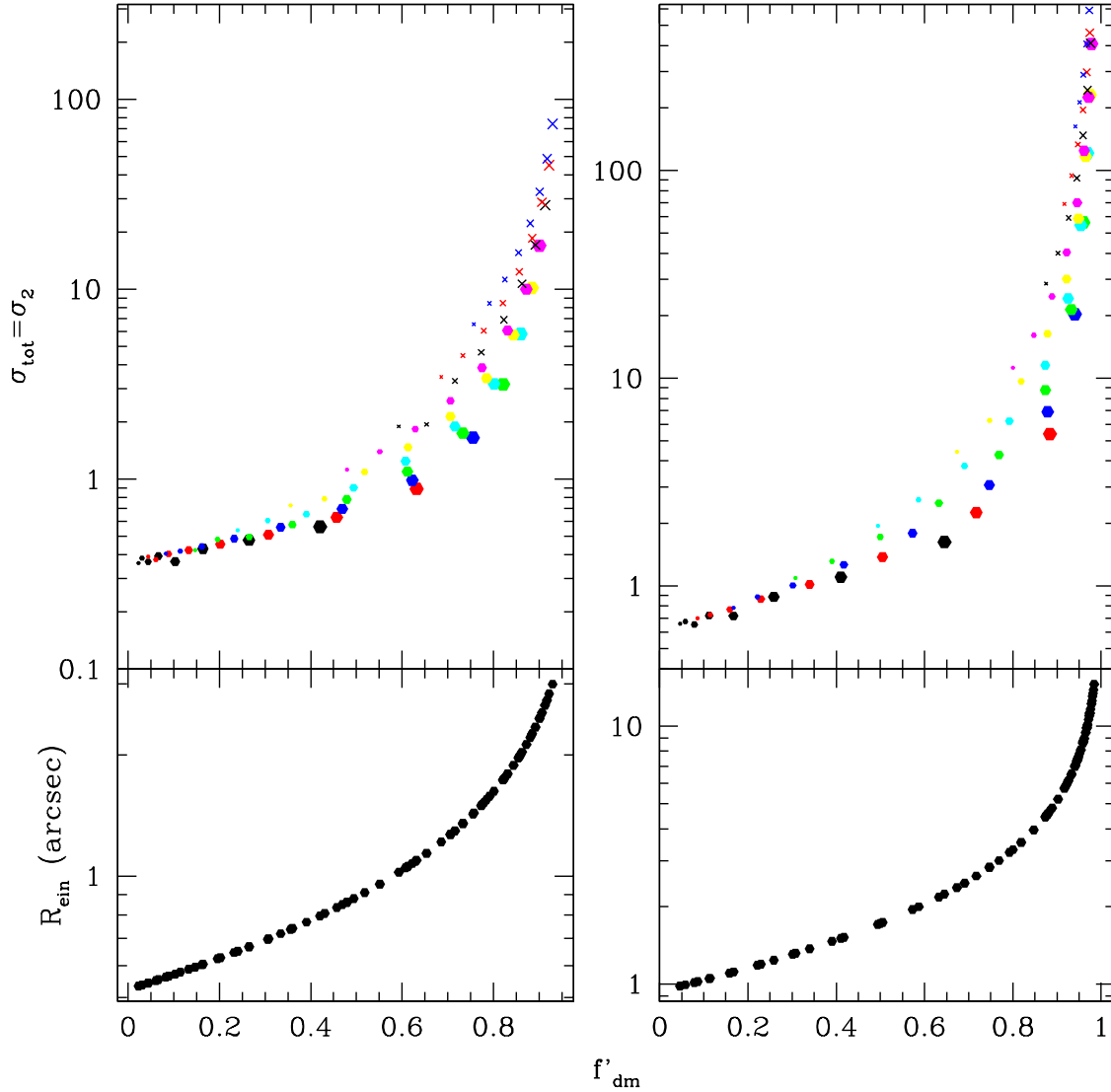


**Figure 8.** For lower (left column) and higher (right column) mass scales, we show: (bottom)—The Einstein radius as a function of the projected dark matter fraction (within the Einstein radius) for all 80 models on the  $\gamma_{\text{dm}}-c_{\text{dm}}$  grid; and (top)—The cross-section as a function of the dark matter fraction. The different point colours and types are the values at fixed  $\gamma_{\text{dm}}$ : hexagons in {black, red, blue, green, cyan, yellow, magenta} for  $\gamma_{\text{dm}} = \{0.00, 0.54, 0.88, 1.14, 1.35, 1.52, 1.66\}$ , and crosses in {black, red, blue} for  $\gamma_{\text{dm}} = \{1.79, 1.90, 2.00\}$ . The symbol sizes from smallest to largest indicate the 8 increasing values of  $c_{\text{dm}}$  at fixed  $\gamma_{\text{dm}}$ .

## 5.2 Varying concentration in the triaxial case

We explore the variation of orientation-averaged cross-sections with dark matter concentration more coarsely for triaxial models, to verify that the trends remain roughly the same as for spherical models. This assumption is acceptable for our coarse grid in  $\gamma_{\text{dm}}$  as presented in Section 4.1, but we need to confirm this for  $c_{\text{dm}}$  as well. Because of the need for 24 viewing angles for any triaxial model, we use only one value of  $\gamma_{\text{dm}} = 1$ , and we restrict the grid in  $c_{\text{dm}}$  to five values ranging from  $-2\sigma$  to  $+2\sigma$  in steps of  $1\sigma$ . Thus for the lower mass scale, we go from  $c_{\text{dm}} = 4.2$  to  $c_{\text{dm}} = 16.8$ ; for the higher mass scale, from  $c_{\text{dm}} = 2.8$  to  $c_{\text{dm}} = 11.2$ . The actual values at the fiducial concentration are given in

Table 2 for all magnification bias modes, so we only present trends relative to those values.

There are several points we infer from the resulting Fig. 9. First, our conclusions from the spherical case are, broadly speaking, robust for the triaxial case: variation of  $c_{\text{dm}}$  with all other parameters fixed leads to enhancements of the total lensing cross-section by factors of a few. In particular, the enhancement can be factors of  $\sim 2$  for the lower mass scale, and  $\sim 4$  for the higher mass scale, where the dark matter component is more important. The reason the range of enhancements is smaller than in Section 5.1 is that the range in  $c_{\text{dm}}$  is smaller; however, the range of enhancements is in line with the spherical case when we restrict the

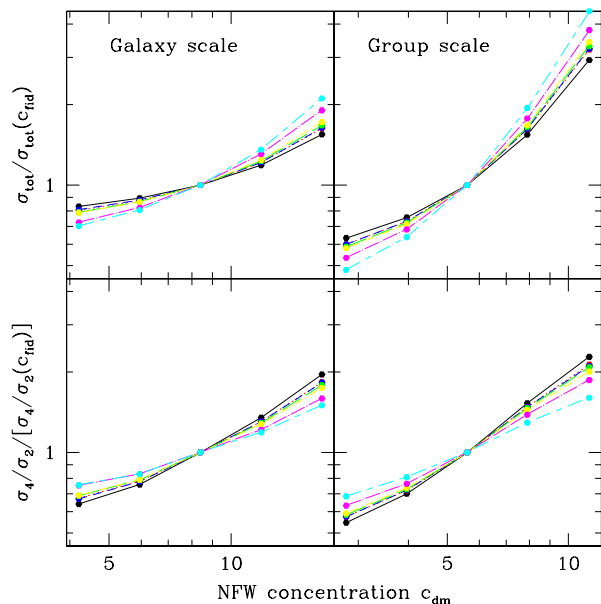


**Figure 9.** For lower (left column) and higher (right column) triaxial mass models, we show the variation of the total, orientation-averaged lensing cross-section (normalised to the value at the fiducial concentration) with concentration in the top panels, and the variation of the 4:2 image ratio with concentration in the bottom panels. Line colours and types indicate the magnification bias mode, as described in the caption for Fig. 1.

grid for the calculations with spherical models in the same way.

One point we were not able to test using the spherical case is the issue of the quad/double ratio  $\sigma_4/\sigma_2$ . Here, we see that this number also can change by factors of a few for reasonable ranges of concentrations for both mass scales. This change presumably results from the fact that the dark matter is intrinsically less round than the stellar component, so increasing the dark matter concentration increases its importance in the inner parts and therefore increases the projected ellipticity of the total mass distribution.

We can also contrast Fig. 9 with the “triaxial” panels of Figs 3 and 4, showing the variation of respectively  $\sigma_{\text{tot}}$  and  $\sigma_4/\sigma_2$  with  $\gamma_{\text{dm}}$  at the fiducial concentration. First, the increase in total lensing cross-section when going from the median concentration to that  $+2\sigma$  is about half the increase when going from  $\gamma_{\text{dm}} = 1$  to  $\gamma_{\text{dm}} = 1.5$ . Second, there are some subtleties that mean that increasing  $\gamma_{\text{dm}}$  and increasing  $c_{\text{dm}}$  do not affect the lensing cross-section in quite the same way. In particular, the ranking of magnification bias modes is different in the two cases: when increasing  $\gamma_{\text{dm}}$ , the  $\sigma_{\text{tot}}$  for the higher flux limit magnification bias modes does not increase as much as for the unbiased case, whereas the opposite is true when increasing  $c_{\text{dm}}$ . Furthermore,  $\sigma_4/\sigma_2$  tends to flatten out when going from  $\gamma_{\text{dm}} = 1$  to  $\gamma_{\text{dm}} = 1.5$ , whereas it increases by a factor of  $\sim 2$  when going from the median concentration to  $+2\sigma$ . Both of these differences between increasing  $\gamma_{\text{dm}}$  and increasing concentration are due to the fact that the biased cross-sections and the four-image cross-section are related not just to the size of the region

in which lensing can occur, but also to the scaling of the surface mass density with radius within this region.

Despite some subtle differences between changing concentration and inner slope, it is clear that in strong lensing-selected analyses, we expect significant selection biases (factors of several) favouring steeper inner slopes  $\gamma_{\text{dm}}$  and higher concentrations  $c_{\text{dm}}$  at fixed mass. This selection bias is manifested not just in  $\sigma_{\text{tot}}$  but also in  $\sigma_4/\sigma_2$ . This result implies that an analysis that recovers the distribution of inner slope and/or concentration with high statistical precision does not measure the intrinsic distribution of these quantities directly, but must account for the selection biases first using simulations.

## 6 DEPROJECTED SÉRSIC DENSITY

In this section, we investigate selection bias with density profile parameters for the composite deprojected Sérsic density profiles. Previous work has characterised the basic lensing properties of spherical, single-component deprojected Sérsic models (Cardone 2004; Baltz et al. 2009), but we study the full lens statistics of two-component spherical and non-spherical models. We divide this analysis into three parts, where we first address the comparison against cusped models in the spherical case; we next consider orientation dependence in the mixed and triaxial cases; and we finally allow the Sérsic index to vary separately for the dark matter and stellar components.

### 6.1 Comparison against cusped models

We first ask whether deprojected Sérsic models lead to significantly different lensing cross-sections compared to cusped models, for both mass scales in the spherical case. This question is important for example in theoretical calculations of the expected number of lenses from a particular strong lensing survey.

The fiducial cusped models with  $\gamma_{\text{dm}} = \{0.5, 1.0, 1.5\}$  have projected dark matter fractions within the corresponding Einstein radii of  $f'_{\text{dm}} = \{0.11, 0.27, 0.62\}$  (lower mass) and  $f'_{\text{dm}} = \{0.18, 0.49, 0.88\}$  (higher mass). The fiducial deprojected Sérsic model has  $f'_{\text{dm}} = 0.55$  and  $f'_{\text{dm}} = 0.85$  for lower and higher mass scales, respectively, which means that qualitatively we expect the Einstein radii and cross-sections to be more comparable to the  $\gamma_{\text{dm}} = 1.5$  cusped model than to the  $\gamma_{\text{dm}} = 1$  case. The results from analytic GRAVLENS calculations show that this expectation is correct: for the lower mass scale,  $\sigma_{\text{tot}} = 1.57 \text{ arcsec}^2$ , comparable to  $\sigma_{\text{tot}} = 1.40 \text{ arcsec}^2$  for the  $\gamma_{\text{dm}} = 1.5$  case, while  $\sigma_{\text{tot}} = 0.53 \text{ arcsec}^2$  for  $\gamma_{\text{dm}} = 1$ . Likewise, for the higher mass scale,  $\sigma_{\text{tot}} = 10.5 \text{ arcsec}^2$ , which is closer to  $\sigma_{\text{tot}} = 15.9 \text{ arcsec}^2$  for the  $\gamma_{\text{dm}} = 1.5$  case than to  $\sigma_{\text{tot}} = 1.63 \text{ arcsec}^2$  for the  $\gamma_{\text{dm}} = 1$  case. All numbers quoted here are unbiased cross-sections, and the trends for  $R_{\text{ein}}$  are similar. We conclude that for the same mass within spheres of over-density  $180\bar{\rho}$ , deprojected Sérsic models with observationally-motivated Sérsic indices and half-mass radii tend to give higher lensing cross-sections than cusped models with the “canonical” inner slope value  $\gamma_{\text{dm}} = 1$ . It is clear that the selection bias with mass for the deprojected Sérsic models is broadly consistent with what one would expect for the cusped models

with  $\gamma_{\text{dm}} = 1.5$ , which is stronger than the selection bias for the  $\gamma_{\text{dm}} = 1$  models.

When we include the effects of magnification bias, we find that the enhancement in the cross-section is similar to the enhancement for the  $\gamma_{\text{dm}} = 1.5$  cusped models. The image separation distributions are fairly narrow as for the cusped models, with a mean of  $1.98 R_{\text{ein}}$  (lower mass) and  $1.88 R_{\text{ein}}$  (higher mass). This result is consistent with our finding in Paper I that the composite deprojected Sérsic model for the galaxy scale is very close to isothermal, whereas the higher mass scale is more dominated by the dark matter and therefore is somewhat less isothermal.

## 6.2 Orientation-dependence

We had found, in Section 3.1, that for the triaxial and mixed shape cusped models, the total unbiased cross-section  $\sigma_{\text{tot}}$  can vary by factors of several when we change the viewing angles. Likewise, the ratio  $\sigma_4/\sigma_2$  can vary from near zero to  $\sim 15$  per cent.

We now compare this result for the orientation dependence in cusped models against the results for the deprojected Sérsic models. We find that the results are very similar for variation of both  $\sigma_{\text{tot}}$  and of  $\sigma_4/\sigma_2$ , which suggests that these numbers do not depend strongly on the functional form of the density profile (for reasonable models). Furthermore, when we include the effects of magnification bias, we find that it changes  $\sigma_{\text{tot}}$  and  $\sigma_4/\sigma_2$  in similar ways as it does for the cusped,  $\gamma_{\text{dm}} = 1.5$  models. This change includes sharp increases in  $\sigma_{\text{tot}}$  and significant enhancement of the quad/double ratio.

When averaging over orientation, we also find that, as for cusped models, the value of  $\sigma_{\text{tot}}$  does not depend strongly on halo shape (when comparing triaxial, mixed, and spherical models).

## 6.3 Sérsic index

In this section, we consider varying the Sérsic indices of both the dark matter ( $n_{\text{dm}}$ ) and stellar component ( $n_*$ ), in the spherical case, for both mass scales. All variation is done at fixed mass. Because an increase in Sérsic index leads to a more highly concentrated profile in the inner regions, we expect that with appropriate normalisation (discussed in Paper I), the lensing cross-section will be an increasing function of Sérsic index. The questions we address are (1) the extent of the selection bias that is possible for a reasonable range of Sérsic indices, and (2) the relative importance of the Sérsic index for each component of the profile. We adopt the ranges in  $n_{\text{dm}}$  and  $n_*$  as derived in Paper I, and sample five values equally in both  $\log n_*$  and  $\log n_{\text{dm}}$ , resulting in a  $5 \times 5$  grid. For  $n_{\text{dm}}$  and  $n_*$  values different from the fiducial values (in the centre of the grid), we change  $\rho_0$  to maintain the total mass and scale radius.

Fig. 10 shows the unbiased cross-section as a function of the Sérsic indices for both mass scales, with contours in the base-10 logarithm relative to the cross-section at the fiducial grid point, i.e.,  $\log(\sigma_{\text{tot}}/\sigma_{\text{tot, fid}})$ . The increase in cross-section with both  $n_{\text{dm}}$  and  $n_*$  is physically understandable. As shown, the total variation on the grid is from  $\sim 0.5$  to  $2\sigma_{\text{tot, fid}}$  for the lower mass scale (factor of 4), or  $\sim 0.45$

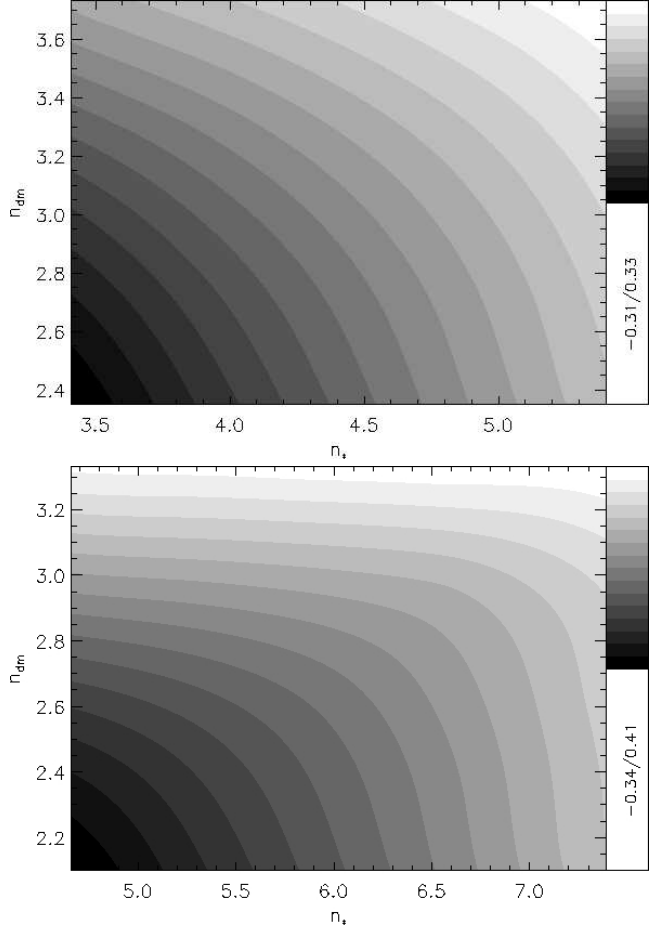


**Figure 10.** Contour plots of the base-10 logarithm of the unbiased cross-section for the lower (top) and higher (bottom) mass scales, relative to the cross-section at the fiducial grid point.

to  $2.6\sigma_{\text{tot, fid}}$  for the higher mass scale (factor of 6). While these increases are significant, they are more comparable to the changes in cross-section for the cusped models when varying  $c_{\text{dm}}$  than varying  $\gamma_{\text{dm}}$ . The reason for this is that changing  $\gamma_{\text{dm}}$  for a cusped model causes a large change in the inner parts of the intrinsic and projected profile, but changing the Sérsic index leads to substantial changes in both the inner and the outer intrinsic profile that partially cancel out when projected along the line-of-sight. The shape of the contours, which run diagonally at low  $n_{\text{dm}}$  and  $n_*$ , but closer to horizontally at high  $n_{\text{dm}}$  and vertically at high  $n_*$ , is also physically understandable: at low  $n_{\text{dm}}$  and  $n_*$ , both components are roughly equally important, whereas at high  $n_{\text{dm}}$ , the stellar component (and therefore  $n_*$ ) is less important, and at high  $n_*$ , the dark matter component (and therefore  $n_{\text{dm}}$ ) is less important. The effect at high  $n_{\text{dm}}$  is more exaggerated for the higher mass scale, because this model was designed to be more dark-matter dominated than the lower mass scale model.

Fig. 11 shows the trends of  $R_{\text{ein}}/R'_{h,*}$  for the lower mass scale on this grid. Note that since we normalise the profiles by fixing the scale radius and mass while varying  $\rho_0$ , the scale radius  $R'_{h,*}$  is the same at each point on the grid, so only  $R_{\text{ein}}$  is varying. The exceptionally horizontal contours require some explanation, since the cross-section contours

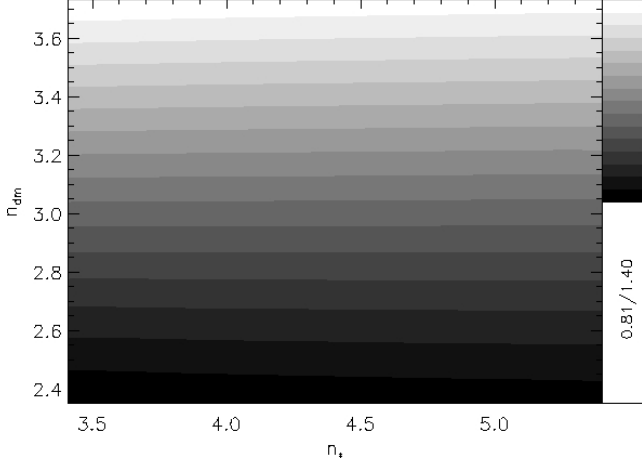


**Figure 11.** Contour plot of  $R_{\text{ein}}/R_{h,*}$  for the lower mass deprojected Sérsic models.

in Fig. 10 are not strictly horizontal. This result can be explained by the deflection curves, shown in Fig. 12 for this mass scale. In this plot, the Einstein radius is where the one-to-one line crosses the  $\alpha(R')$  curves for the composite models, and as we have already seen, these crossings occur in nearly the same place. This results from our normalisation convention, which fixes the same half-mass radius  $R'_{h,*}$  for each of the  $n_*$  values, meaning that it fixes the average convergence  $\bar{\kappa}(R'_{h,*})$  and therefore the deflection at  $R'_{h,*}$ ,  $\alpha = R'_{h,*}\bar{\kappa}(R'_{h,*})$ , to the same value. Because the DM component is also fixed, it means that the models with different  $n_*$  have the same  $R_{\text{ein}}$  and the same  $f'_{\text{dm}}$  within  $R_{\text{ein}}$ . However, this is purely a consequence of our chosen redshifts and the balance of stellar and dark matter in our models; had we arranged it so that  $R_{\text{ein}} \ll R'_{h,*}$ , then  $n_*$  would indeed affect  $R_{\text{ein}}$ . However, the cross-sections do not have to be the same despite identical  $R_{\text{ein}}$  values for varying  $n_*$ , because they are set by the outer (source-plane) caustic, which is related to the inner (lens-plane) critical curve, determined by the *slope* of the deflection on small scales. Clearly, in Fig. 12, while the deflections are the same at  $R_{\text{ein}}$ , their slopes are quite different within  $R_{\text{ein}}$ , leading to different lensing cross-sections. Finally, we note that despite our superimposing two non-trivially complicated deprojected Sérsic models to make the composite galaxy model, the deflection curve for the composite model is remarkably close to the flat, isothermal case ( $\alpha = R_{\text{ein}}$ ), which we have also seen with the cusped models. This fact explains the very narrow image separation distribution for all of these composite models.

Finally, we consider the selection bias trends for biased cross-sections, particularly the one using the highest flux limit and total magnification. That trend is presented for the lower mass scale in Fig. 13, and shows that the shape of the contours is quite different from the unbiased case (Fig. 10, top panel). While  $n_{\text{dm}}$  has the same, significant effect on the cross-section as in the unbiased case, the effect is much less significant for  $n_*$  and has changed sign: stellar components that are less concentrated give slightly higher biased cross-sections. While there is no simple, physical explanation for this result, it is apparently related to the scaling of the convergence within the Einstein radius, and the fact that a very concentrated (high  $n_*$ ) stellar component only has a

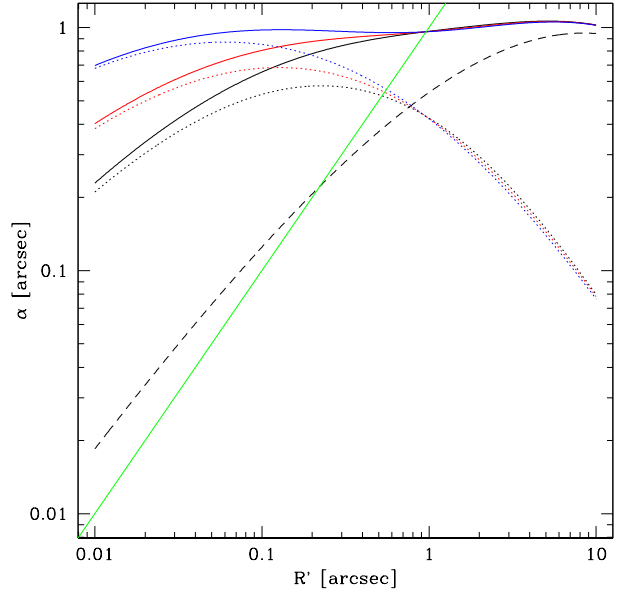


**Figure 12.** Deflection as a function of scale for the lower mass deprojected Sérsic mass model. The black dashed line is for the fiducial DM component; the black, red, and blue dotted lines are for the stellar components with the lowest, fiducial, and highest  $n_*$ ; and the black, red, and blue solid lines are the corresponding composite models (stellar plus DM). Finally, the green solid line corresponds to  $\alpha = R'$ ; the intersection of this line with the deflection curves occurs at  $R_{\text{ein}}$ .

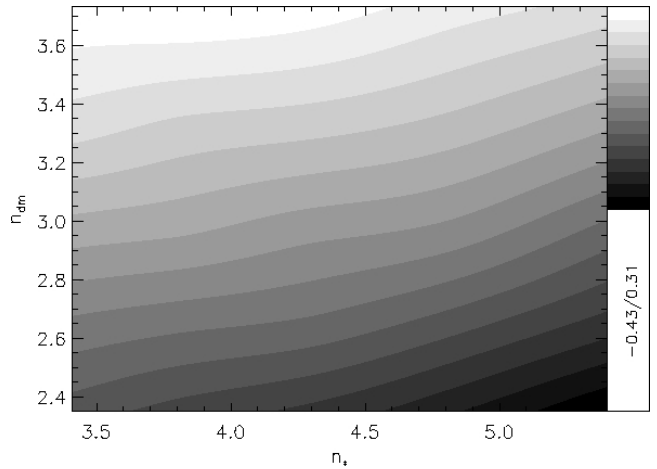


**Figure 13.** Contour plot of the base-10 log of the biased cross-section for the lower mass scale, relative to this cross-section at the fiducial grid point.

very small region where the convergence is extremely high, whereas a less concentrated one has a larger area where it is fairly high, which turns out to be more important for these very biased cross-sections.

## 7 ROBUSTNESS OF CONCLUSIONS TO CHANGES IN REDSHIFT

Finally, to ascertain how much our conclusions about selection biases in the previous sections depend on our chosen fiducial lens and source redshifts, we now try varying the redshifts in several ways.

If we vary both the lens and the source redshifts in a way that preserves  $\Sigma_c$ , then the physical scale within the galaxy that is measured by strong lensing is the same, but it will lead to different image separation distributions, scaled by the angular diameter distance  $D_L$  of the lens galaxy. This change may lead to *observational* selection effects that depend sensitively on the survey image search strategy (resolution and maximum angular separation), but no physical selection effects, so we do not attempt to model this in any general way.

Now consider fixing the lens redshift (and therefore the conversion from physical to angular scale), but shifting the source redshift to rescale the critical surface mass density  $\Sigma_c$ . This shift will change the Einstein radius  $R_{\text{ein}}$  and therefore the physical scale of the density profile that is probed by strong lensing. Thus, this change may result in different *physical* selection biases.

If we fix the lens redshift to our fiducial  $z_L = 0.3$  but move the source redshift considerably lower, from the fiducial  $z_S = 2.0$  to  $z'_S = 0.6$ , then the critical surface density increases by  $\sim 70$  per cent. This change means that the strong lensing is due to smaller scales, where the average projected surface density is higher, and that the lensing cross-section for this density profile will be lower. Because of the importance of smaller scales, the projected dark matter fraction  $f'_{\text{dm}}$  will decrease. As a test, we recompute  $R_{\text{ein}}$  and the lensing cross-sections for both mass scales as a function of the dark matter halo inner slope  $\gamma_{\text{dm}}$  to see the degree to which the selection bias we identified with our fiducial lens and source redshifts persist. We also increase the resolution of the surface density maps used by GRAVLENS for these calculations by a factor of two, while maintaining the box size, to ensure that the critical curves can be properly resolved.

We also consider a value of  $\Sigma_c$  that is 40 per cent lower than our fiducial value. While this low  $\Sigma_c$  does not correspond to any sensible value of  $z_S$  for our fiducial  $z_L$ , we assume a higher  $z_L \sim 0.6$  and  $z_S \sim 3$ . Because of the different  $z_L$ , all angular scales output by our pipeline must be rescaled by  $D_A(z = 0.3)/D_A(z = 0.6) = 0.66$ , i.e., the Einstein radii must be rescaled by 0.66 and the cross-sections by  $0.66^2$ . However, the relevant quantities for selection bias associated with true variation of galaxy density profiles, e.g.  $f'_{\text{dm}}$ , are preserved. Since we expect increased Einstein radii and cross-sections, we preserve the resolution but increase the box size by a factor of 2.

Table 3 shows what happens to relevant quantities for lensing when we vary  $\Sigma_c$  to values 70 per cent higher and 40 per cent lower. We consider only the unbiased cross-sections for the spherical shape model. First, we can see that when we increase (decrease)  $\Sigma_c$ , we decrease (increase)  $R_{\text{ein}}$  and  $f'_{\text{dm}}$ , as expected. The change in  $R_{\text{ein}}$  can be significant, up to a factor of  $\sim 2$  for the changes in  $\Sigma_c$  that we have tested. We find that the selection bias with  $\gamma_{\text{dm}}$ , represented in the last two rows of this table, is nearly independent of  $\Sigma_c$  for  $\gamma_{\text{dm}}$  below the fiducial value of 1, and for higher  $\gamma_{\text{dm}}$

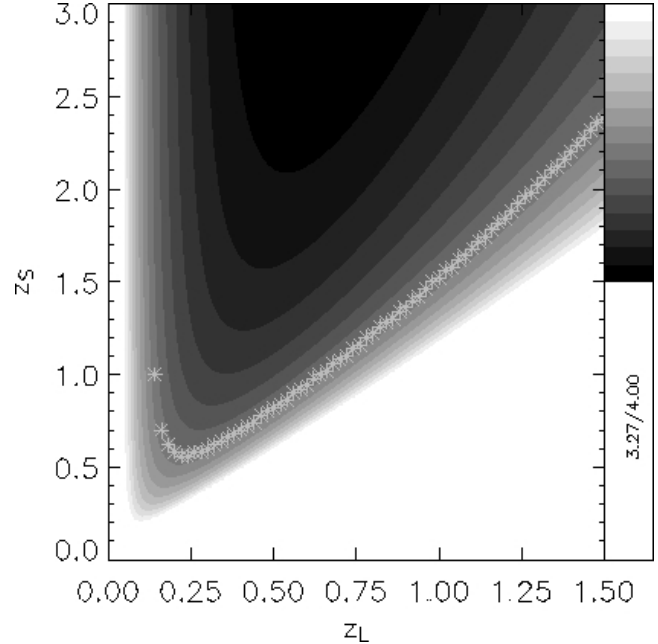


**Figure 14.** Critical surface density, plotted as  $\log[\Sigma_c/(M_\odot/\text{pc}^2)]$ , as a function of lens and source redshift. For  $z_S < z_L$ , where  $\Sigma_c$  is formally infinite, we have set it to the maximum value shown,  $10^4 M_\odot/\text{pc}^2$ . Asterisks indicate the minimum source redshift for a given lens redshift for which we have confirmed that our conclusions about selection bias are valid.

it is a slightly increasing function of  $\Sigma_c$ . The sign of this change is surprising, in the sense that if  $f'_{\text{dm}}$  is lower than we might naively expect the parameters of the dark matter distribution to be less significant. However, we can explain this change by the fact that the cross-section  $\sigma_{\text{tot}}$  is determined by the outer (source-plane) caustic, which relates to the inner (lens-plane) critical curve. This in turn is determined by the slope of the density profile on small scales, so if the lensing properties are determined by smaller (larger) physical scales, as when we increase (decrease)  $\Sigma_c$ , then  $\gamma_{\text{dm}}$  becomes more (less) important and selection bias becomes stronger (weaker).

However, it is encouraging that the selection bias only changes by +14 and  $-4$  per cent (+41 and  $-13$  per cent) for changes in  $\Sigma_c$  of +70 and  $-40$  per cent for the lower (higher) mass model. This result suggests that within the range of  $\Sigma_c$  that we have considered in this subsection, the conclusions of our paper regarding physical selection bias are not strongly dependent on our choice of fiducial lens and source redshifts. (The same is not true for observational selection biases, which may be strongly affected by changing  $z_L$  and thus the characteristic angular scale of the system.) On Fig. 14, we have indicated the lens and source redshift combinations for which our conclusions are robust according to the tests in this subsection.

We must also consider the issue of magnification bias. Magnification bias complicates a change in the redshift of the system in two ways. First, if the source redshift is different, then for a given survey flux limit, the luminosity threshold is different. For a broken power-law luminosity function that is steeper at the bright end, this means that if

**Table 3.** Summary of the lensing results for the cusped, spherical model when varying  $\Sigma_c$  so that different physical scales are probed. The factor of 0.66 in  $R_{\text{ein}}$  for the lower  $\Sigma_c$  cases is shown separately since it is not indicative of the physical scale within the galaxy.

Quantity	Fiducial $\Sigma_c$	Higher $\Sigma_c$	Lower $\Sigma_c$
Lower mass scale			
$R_{\text{ein}}(\gamma_{\text{dm}} = 0.5)$	0.58	0.36	$0.79 \times 0.66 = 0.52$
$R_{\text{ein}}(\gamma_{\text{dm}} = 1.0)$ (arcsec)	0.68	0.41	$0.95 \times 0.66 = 0.63$
$R_{\text{ein}}(\gamma_{\text{dm}} = 1.5)$	1.04	0.61	$1.46 \times 0.66 = 0.97$
$f'_{\text{dm}}(R' < R_{\text{ein}}, \gamma_{\text{dm}} = 0.5)$	0.13	0.08	0.17
$f'_{\text{dm}}(R' < R_{\text{ein}}, \gamma_{\text{dm}} = 1.0)$	0.28	0.20	0.37
$f'_{\text{dm}}(R' < R_{\text{ein}}, \gamma_{\text{dm}} = 1.5)$	0.60	0.51	0.67
$\sigma_{\text{tot}}(\gamma_{\text{dm}} = 0.5)/\sigma_{\text{tot}}(\gamma_{\text{dm}} = 1.0)$	0.79	0.79	0.79
$\sigma_{\text{tot}}(\gamma_{\text{dm}} = 1.5)/\sigma_{\text{tot}}(\gamma_{\text{dm}} = 1.0)$	2.65	2.96	2.51
Higher mass scale			
$R_{\text{ein}}(\gamma_{\text{dm}} = 0.5)$	1.18	0.63	$1.73 \times 0.66 = 1.14$
$R_{\text{ein}}(\gamma_{\text{dm}} = 1.0)$ (arcsec)	1.75	0.88	$2.75 \times 0.66 = 1.82$
$R_{\text{ein}}(\gamma_{\text{dm}} = 1.5)$	4.44	2.33	$6.75 \times 0.66 = 4.46$
$f'_{\text{dm}}(R' < R_{\text{ein}}, \gamma_{\text{dm}} = 0.5)$	0.22	0.13	0.30
$f'_{\text{dm}}(R' < R_{\text{ein}}, \gamma_{\text{dm}} = 1.0)$	0.51	0.36	0.63
$f'_{\text{dm}}(R' < R_{\text{ein}}, \gamma_{\text{dm}} = 1.5)$	0.87	0.80	0.91
$\sigma_{\text{tot}}(\gamma_{\text{dm}} = 0.5)/\sigma_{\text{tot}}(\gamma_{\text{dm}} = 1.0)$	0.52	0.51	0.52
$\sigma_{\text{tot}}(\gamma_{\text{dm}} = 1.5)/\sigma_{\text{tot}}(\gamma_{\text{dm}} = 1.0)$	9.19	12.9	8.04

the source is more distant, the limiting luminosity becomes brighter, so the actual number of lensing systems is modulated due to both the different number density of sources above that limit and by the change in effective  $\sigma_{\text{tot}}$  due to the steeper luminosity function at the limit. Second, since the source luminosity function may be a function of redshift, we anticipate that the biased cross-sections, which are the relevant quantity for any particular survey given its flux limit and search strategy, may also change due to this effect. For our analysis in this section, we have ignored this change in the magnification bias formalism, but to determine the cross-sections for a real survey this evolution would have to be taken into account. In any case, both of these magnification bias effects qualify as observational rather than physical selection biases that are more properly simulated in the context of a particular strong lensing survey.

## 8 CONCLUSIONS

Using the pipeline developed in Paper I, we have presented a series of tests for selection biases in point-source strong lensing surveys due to physical differences between galaxy or group mass systems. These tests reveal whether the distribution of physical parameters, such as profiles and shapes of (projected) densities, in strong lensing systems reflects that distribution among the galaxy population in general.

We have attempted to distinguish between physical selection biases which relate to the parameters of the galaxy density, versus observational selection biases which depend on the lensing detection strategy (specifically, the flux limit, angular resolution, and maximum angular separation for detection of a lensing system). The former can be understood for lensing surveys in general, whereas the latter need to be simulated on a case-by-case basis.

To organize our conclusions, we first give a sample application to illustrate how our analysis may be applied to real lens surveys, then give a more complete list of our con-

clusions about selection biases in strong lensing surveys, and finally give a more general discussion of our results.

### 8.1 Example application

As an example of how this work may be applied to the analysis of real data, we consider the joint distribution of  $c_{\text{dm}}$  and  $\gamma_{\text{dm}}$  and show how the distribution that would be observed in some strong lensing survey is related to the intrinsic distribution. In this example we use the spherical higher mass model. The concentration is known from  $N$ -body simulations to have a lognormal distribution at fixed mass (e.g., Bullock et al. 2001). The distribution of the logarithmic slope is not well known, however, because of difficulties in resolving small scales. Indeed, some recent work has suggested that DM halo profiles do not converge to a single asymptotic logarithmic slope (e.g., Navarro et al. 2004), although even in that case one can imagine constraining (in both simulations and real data) the inner slope at some fixed fraction of the virial radius and calling that  $\gamma_{\text{dm}}$ . We assume, for illustration, that this procedure may give a mean  $\langle \gamma_{\text{dm}} \rangle = 1$  and a Gaussian scatter of 0.25. We expect that any constraints on  $\gamma_{\text{dm}}$  and  $c_{\text{dm}}$  based on measuring enclosed mass will cause  $\gamma_{\text{dm}}$  and  $c_{\text{dm}}$  to be anti-correlated, so we assume a correlation coefficient of  $-0.3$  between  $\gamma_{\text{dm}}$  and  $\ln(c_{\text{dm}})$ . We emphasize that the  $\gamma_{\text{dm}}$  distribution and the correlation coefficient are merely guesses made for the purpose of this exercise, which means that our results should *not* be taken as a prediction for what would be seen in reality; they are intended just to be a useful illustration.

Fig. 15 shows our assumed intrinsic distribution (lower right panel), along with the distribution that would be observed among lens galaxies (upper right panel). The two distributions are related via the lensing selection function shown in Fig. 7. (For this exercise we use the selection function without magnification bias.) Lensing selection effects clearly shift the peak of the joint distribution to higher val-

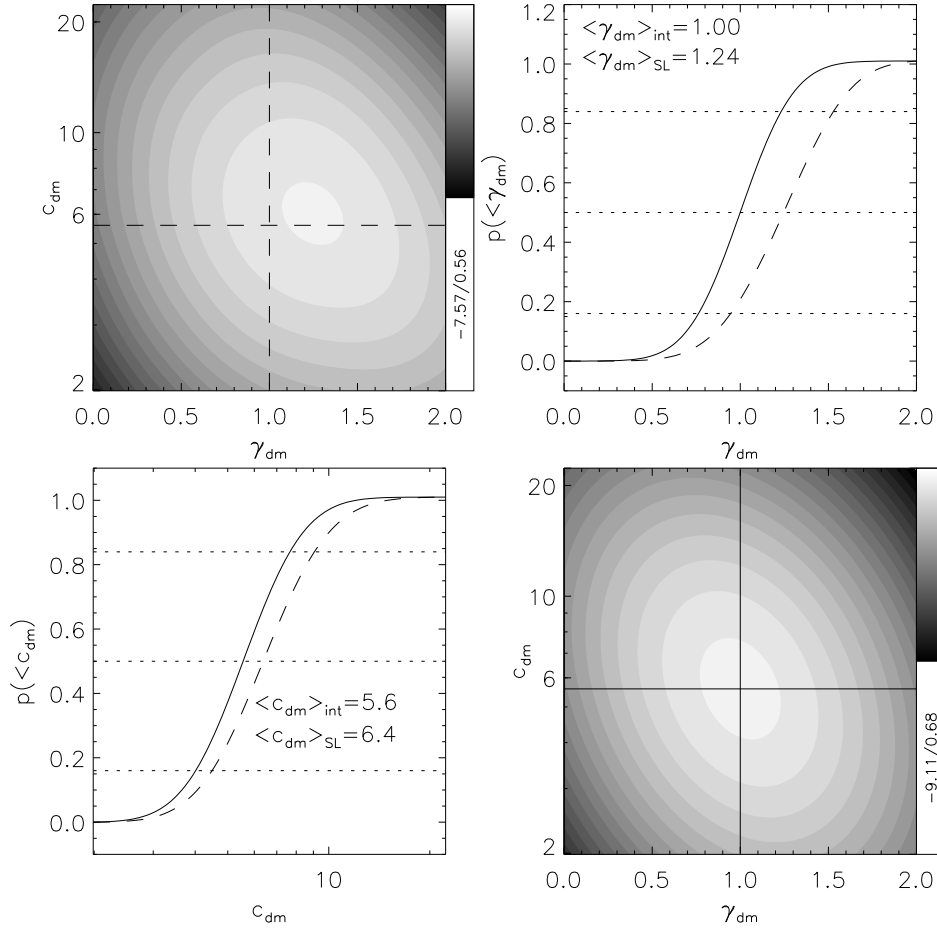


**Figure 15.** Illustration of the procedure for removing the effects of lensing selection bias from the observed distribution of parameters, shown for the spherical, higher mass model. The top left panel shows the joint distribution  $p_{\text{SL}}(\gamma_{\text{dm}}, c_{\text{dm}})$  as it may be observed in some strong lensing survey. The bottom right panel shows the corresponding intrinsic distribution  $p_{\text{int}}(\gamma_{\text{dm}}, c_{\text{dm}})$ , which would be recovered from the observed distribution by removing the selection bias function shown in Fig. 7. In both cases the grayscale and contours are logarithmic, and the horizontal and vertical lines are drawn at the median values of  $\gamma_{\text{dm}}$  and  $c_{\text{dm}}$  for the *intrinsic* distribution. We emphasize that the intrinsic joint distribution is not well known from observations or simulations, so we have constructed a simple example for illustration (see text for more discussion); thus, this figure should *not* be taken as a prediction for what will be seen in lensing surveys. The top right and bottom left panels show cumulative distributions for  $\gamma_{\text{dm}}$  and  $c_{\text{dm}}$  (respectively) obtained by taking slices through the joint distributions the intrinsic median values of  $c_{\text{dm}}$  or  $\gamma_{\text{dm}}$ . In each case the dashed line represents the “observed” distribution while the solid line represents the recovered intrinsic distribution. The dotted horizontal lines indicate the median and  $\pm 1\sigma$  range.

ues of  $\gamma_{\text{dm}}$  and  $c_{\text{dm}}$ . To further quantify the effects, we also show 1-d slices through the joint distribution at fixed values of  $\gamma_{\text{dm}}$  or  $c_{\text{dm}}$ . These plots demonstrate that the  $\gamma_{\text{dm}}$  and  $c_{\text{dm}}$  distributions are both shifted and broadened in the “observed” distribution compared with the intrinsic distribution. In particular, the mean and median values are shifted by 24 ( $\gamma_{\text{dm}}$ ) and 14 ( $c_{\text{dm}}$ ) per cent. Consequently, any attempt to recover the mean of  $c_{\text{dm}}$  and/or  $\gamma_{\text{dm}}$  for some sample of strong lenses need to be corrected for selection bias before comparing against predictions that were made for a more general galaxy sample.

## 8.2 Summary

The biases in  $\gamma_{\text{dm}}$  and  $c_{\text{dm}}$  are just one example of the physical selection effects we have explored. Here is a more complete list of our main conclusions:

- There is a strong preference for lensing systems to be at higher mass. This trend is counterbalanced by the strongly decreasing mass function at high mass, but will nonetheless significantly increase the mean mass for lensing systems relative to that for all galaxies. The degree of preference depends sensitively on how the mass is distributed in the inner parts of the galaxy, and on the details of the magnification bias (flux limit and detection strategy). [Section 2.4]
- Lensing systems show a significant preference for certain orientations, with factors of 2–3 variation in lensing

cross-sections depending on their shape. In particular, the total cross-section is maximised when the surface mass density is maximised, i.e., when the galaxy is viewed with the long axis along the line of sight; and the four-image cross-section is maximised when the projected ellipticity is maximised, i.e., when the intermediate axis aligns with the line of sight. [Sections 3.1 and 6.2]

- The total, orientation-averaged lensing cross-section is not strongly dependent on the intrinsic shape of the galaxy. In contrast, the quad/double ratio may be a powerful probe of the distribution of the shape of the mass density in the inner parts of galaxies, although it also has a strong dependence on observational issues such as the source luminosity function. [Section 3.2]

- An observational scarcity of three-image lens systems may place a strong constraint on the abundance of strongly oblate matter distributions. [Section 3.2]

- Statistical variations in the dark matter density properties, such as the inner slope  $\gamma_{\text{dm}}$  and the concentration  $c_{\text{dm}}$ , may lead to a strong selection bias amounting to factors of many in  $\sigma_{\text{tot}}$ , and to tens of per cent variation in  $\sigma_4/\sigma_2$ , nearly independent of the shape of the galaxy model and the observational issues relating to the magnification bias. Consequently, even if analyses are able to break the degeneracy between these parameters, for example using strong lensing plus some other technique to measure the profile at larger scales, they still cannot claim to measure the intrinsic distribution of these quantities directly. [Sections 4.1, 5.1, and 5.2]

- Adiabatic contraction has a less significant effect on the lensing cross-section than increasing the dark matter inner slope for a generalised NFW model from  $\gamma_{\text{dm}} = 1$  to  $\gamma_{\text{dm}} = 1.5$ . However, the increase may still be a factor of two, which means that if galaxy formation scenarios dictate whether AC occurs, there may be a selection bias towards those galaxies that have undergone significant adiabatic contraction, and against those that have not. [Sections 4.1 and 4.3]

- The lensing cross-sections of deprojected Sérsic models depend on the indices  $n_*$  of the stellar and  $n_{\text{dm}}$  of the dark matter component. Higher Sérsic indices correspond to a more concentrated profile and therefore a higher lensing cross-section at fixed mass. Reasonable changes of these indices, within the observational scatter, can change the lensing cross section by factors of several. For the fiducial Sérsic model,  $R_{\text{ein}}$  and  $\sigma_{\text{tot}}$  are higher than for cusped models with the “canonical” inner slope value  $\gamma_{\text{dm}} = 1$ , and closer to those for the  $\gamma_{\text{dm}} = 1.5$  cusped model. [Section 6]

- While varying the lens and source redshifts changes the range of physical scales probed using strong lensing, we have found that the dependence on  $\Sigma_c$  is not very strong, and therefore that our conclusions regarding the extent of selection biases are valid for a wide range of lens-source redshift combinations (Fig. 14). Furthermore, our results suggest that the physical selection bias is modified (when changing lens and/or source redshift) such that the very inner part of the profile is more (less) important if  $\Sigma_c$  is higher (lower), making selection bias more (less) important than for our fiducial combination of lens and source redshifts. [Section 7]

### 8.3 Discussion

Where possible, we have compared our conclusions on physical selection biases with earlier papers in the relevant sections. In general our conclusions are consistent with those of previous studies, but our pipeline allows a more unified approach to selection biases in lensing surveys while using realistic galaxy models. This unified approach allows for non-trivial extensions of previous results, to two-component models, different profile types, and more shapes than were used in previous studies. Furthermore, we can understand trends seen in strong lens analyses based on N-body plus semi-analytic modeling (Hilbert et al. 2007; Möller et al. 2007; Hilbert et al. 2008) in terms of the interplay between different types of selection biases. For example, the tendency found by Möller et al. (2007) for quad lenses to have a pronounced disk component comes from an interplay between mass bias, shape bias, and orientation bias, as discussed in Section 3.2.2. A comparison with previous results also teaches us lessons about the limitations of these simple models: for example, that when estimating selection biases with dark matter halo parameters, we must include a baryonic component so that we do not overestimate the severity of the selection bias, as discussed in Sections 4.1 and 5.1.

Finally, our work has revealed a number of useful points related to the interpretation of observational strong lensing results in general. For example, despite the relative complexity of our mass models, the image separation distribution in all cases has a mean near  $2R_{\text{ein}}$  and a fairly small width (Section 4.2), as in the isothermal case. The dependence of this distribution on magnification bias is a very small effect. On a related note, these models are very close to isothermal near  $R_{\text{ein}}$  despite strong variations at smaller or larger scales (see paper I figure 5), so a measurement to constrain the slope of the projected density profile at  $R_{\text{ein}}$  does not allow discrimination between profiles with different  $\gamma_{\text{dm}}$  or  $c_{\text{dm}}$ , unless another technique is used to constrain the profile independently on much smaller or larger scales (see also Paper I). Note, however, that because of the significant deviations from isothermality on other scales, these models have very different relationships between  $R_{\text{ein}}$  and  $\sigma_{\text{tot}}$  than for an isothermal model (see also Table 1).

We can apply several of our conclusions to previously-published work. For example, Koopmans et al. (2006) use a joint lensing and kinematics analysis of 15 SLACS lenses to infer that the average slope of the 3d density profile near the Einstein radius is  $\langle\gamma\rangle = 2.01^{+0.02}_{-0.03}$  (68 per cent CL), with intrinsic rms scatter of 0.12. We defer the consideration of possible modeling biases to future work, and consider the possible impact of selection biases here. This extremely high level of isothermality is, at first glance, surprising; but then we realise from paper I figures 5 and 7 that in fact many different combinations of stellar and DM models can conspire to yield a total model that is nearly isothermal over a range of scales including the Einstein radius. Consequently, a measurement of the total density profile in the vicinity of the Einstein radius cannot, on its own, uniquely determine the form of the DM profile. However, once Koopmans et al. (2006) impose a prior on the stellar mass-to-light ratio they are able to constrain the projected dark matter fraction, which (in combination with knowledge of the projected lu-

minosity profile) might provide constraints on the inner dark matter profile. However, due to the partial degeneracy between mass,  $\gamma_{\text{dm}}$  and  $c_{\text{dm}}$  in strong lensing properties, this constraint does not allow for an explicit determination of the dark matter profile parameters without additional constraints from larger radii. In other words, there are many models in that three-dimensional space that would give the observed  $R_{\text{ein}}$  and  $f'_{\text{dm}}$ .

There are a number of selection bias-related problems that involve a higher level of complexity and that we have therefore reserved for future work. These include, but are not limited to: (i) the effect of varying stellar mass-to-light ratios for a given galaxy model; (ii) modeling satellite galaxies that have their own stellar and dark matter components but are distributed within the halo of a group or cluster (rather than residing at the centre), and may have the dark matter and/or stars tidally stripped; (iii) lensing of extended sources rather than point sources, for which the basic trends should be qualitatively similar, but for which observational selection effects and observing conditions are crucial; (iv) more useful ways of quantifying image separation distributions for systems with more than two images, and what information can be learned in this way; (v) intrinsic misalignment of the non-spherical dark matter and stellar components, warps, and other more complex shape models.

In addition to this future work on selection biases, we also have designed this pipeline so that it can be easily adapted to study modeling biases, which can occur when using overly simplified mass models. Work on modeling biases can be extended to include strong + weak lensing analyses, as can be done at cluster mass scales. With the addition of kinematics, we can study modeling biases not just in strong lensing systems, but also in kinematic and in kinematic + strong lensing analyses. In short, this pipeline should be a useful tool in understanding the analysis requirements for current and future strong lensing, kinematics, and weak lensing surveys that aim to understand galaxy density profiles.

Finally, we note that considerable additional work would be necessary to use these results to estimate selection biases in a real survey. For example, observational selection biases need to be accounted for. This may include the imposition of a maximum or a minimum angular separation between images depending on the use of an aperture or a resolution-limited approach, respectively. For an example of work considering these and related issues, see Kochanek (1991). While this may change the effects of physical selection biases, either enhancing or counteracting them, it can also alter the lens redshift distribution by favouring higher or lower redshifts, respectively, due to the conversion between angular and physical scale. Furthermore, the evolution of the survey flux limit with the source redshift distribution must be taken into account: we have considered a fixed *luminosity* limit, but a typical flux-limited survey would have a variable luminosity limit that gets brighter for higher redshift, altering the biased cross-sections as a function of source redshift even if the source luminosity function is assumed to be independent of redshift. This will tend to push the source galaxy population to higher redshifts on average.

Another point is that we have not attempted to model the full intrinsic distribution of galaxy properties,  $p_{\text{int}}(\vec{x})$ . We have studied instead the (physical) mapping function  $\sigma(\vec{x})$  that determines the final observed strong lensing popu-

lation from the intrinsic one. To predict strong lensing populations would require a full simulation of the intrinsic galaxy property distribution  $p_{\text{int}}(\vec{x})$ , which is clearly beyond the scope of this paper, but which has been attempted in limited form using N-body simulations plus semi-analytic models by Hilbert et al. (2007), Möller et al. (2007), and Hilbert et al. (2008). In short, a full simulation of the lens galaxy population and source quasar population would be necessary to estimate the parameters of the strong lensing galaxy population in detail for a particular survey. Nonetheless, our work is an important first step in unraveling and disentangling physical sources of selection biases for current and future strong lensing surveys.

## ACKNOWLEDGEMENTS

We are thankful to Chung-Pei Ma, Michael Kuhlen and Scott Tremaine for stimulating discussions on related topics. We thank the referees for constructive comments and suggestions. This work has made use of the public CONTRA software package provided by Oleg Gnedin to perform adiabatic contraction calculations.

RM and GvdV acknowledge support provided by NASA through Hubble Fellowship grants HST-HF-01199.02-A and HST-HF-01202.01-A (respectively), awarded by the Space Telescope Science Institute, which is operated by the Association of Universities for Research in Astronomy, Inc., for NASA, under contract NAS 5-26555. CRK acknowledges support from NSF through grant AST-0747311, and from NASA through grant HST-AR-11270.01-A from the Space Telescope Science Institute, which is operated by the Association of Universities for Research in Astronomy, Inc., under NASA contract NAS 5-26555.

## REFERENCES

- Baltz E. A., Marshall P., Oguri M., 2009, JCAP, 1, 15
- Blumenthal G. R., Faber S. M., Flores R., Primack J. R., 1986, ApJ, 301, 27
- Bolton A. S., Burles S., Koopmans L. V. E., Treu T., Gavazzi R., Moustakas L. A., Wayth R., Schlegel D. J., 2008, ApJ, 682, 964
- Browne I. W. A. et al. 2003, MNRAS, 341, 13
- Bullock J. S., Kolatt T. S., Sigad Y., Somerville R. S., Kravtsov A. V., Klypin A. A., Primack J. R., Dekel A., 2001, MNRAS, 321, 559
- Cardone V. F., 2004, A&A, 415, 839
- Chae K.-H., 2003, MNRAS, 346, 746
- Ciotti L., Bertin G., 1999, A&A, 352, 447
- Comerford J. M., Natarajan P., 2007, MNRAS, 379, 190
- Dobler G., Keeton C. R., Bolton A. S., Burles S., 2008, ApJ, 685, 57
- Falco E. E. et al, 2001, in Astronomical Society of the Pacific Conference Series, Vol. 237, Brainerd T. G., Kochanek C. S., eds., 25
- Fassnacht C. D., Marshall P. J., Baltz A. E., Blandford R. D., Schechter P. L., Tyson J. A., 2004, in Bulletin of the American Astronomical Society, 36, 1531
- Fedeli C., Bartelmann M., Meneghetti M., Moscardini L., 2007, A&A, 473, 715

- Ferrarese L. et al. 2006, ApJS, 164, 334  
 Fukugita M., Turner E. L., 1991, MNRAS, 253, 99  
 Gnedin O. Y., Kravtsov A. V., Klypin A. A., Nagai D., 2004, ApJ, 616, 16  
 Hernquist L., 1990, ApJ, 356, 359  
 Hilbert S., White S. D. M., Hartlap J., Schneider P., 2007, MNRAS, 382, 121  
 Hilbert S., White S. D. M., Hartlap J., Schneider P., 2008, MNRAS, 386, 1845  
 Huterer D., Keeton C. R., Ma C.-P., 2005, ApJ, 624, 34  
 Huterer D., Ma C.-P., 2004, ApJ, 600, L7  
 Inada N. et al. 2008, AJ, 135, 496  
 Jiang G., Kochanek C. S., 2007, ApJ, 671, 1568  
 Kauffmann G. et al. 2003, MNRAS, 341, 33  
 Keeton C. R., 2001a, ApJ, 561, 46  
 —, 2001b, preprint (astro-ph/0102340)  
 Keeton C. R., Kochanek C. S., 1998, ApJ, 495, 157  
 Keeton C. R., Kochanek C. S., Seljak U., 1997, ApJ, 482, 604  
 Keeton C. R., Madau P., 2001, ApJ, 549, L25  
 Keeton C. R., Zabludoff A. I., 2004, ApJ, 612, 660  
 Keeton C. R. I., 1998, PhD thesis  
 Kochanek C. S., 1991, ApJ, 379, 517  
 —, 1996, ApJ, 473, 595  
 —, 2006, in Saas-Fee Advanced Course 33: Gravitational Lensing: Strong, Weak and Micro, Meylan G., Jetzer P., North P., Schneider P., Kochanek C. S., Wambsganss J., eds., 91  
 Kochanek C. S., White M., 2001, ApJ, 559, 531  
 Koopmans L. V. E., Browne I. W. A., Jackson N. J., 2004, New Astronomy Review, 48, 1085  
 Koopmans L. V. E., Treu T., Bolton A. S., Burles S., Moustakas L. A., 2006, ApJ, 649, 599  
 Kuhlen M., Keeton C. R., Madau P., 2004, ApJ, 601, 104  
 Li L.-X., Ostriker J. P., 2002, ApJ, 566, 652  
 Maller A. H., Flores R. A., Primack J. R., 1997, ApJ, 486, 681  
 Mandelbaum R., Seljak U., Kauffmann G., Hirata C. M., Brinkmann J., 2006, MNRAS, 368, 715  
 Marshall P., Blandford R., Sako M., 2005, New Astronomy Review, 49, 387  
 Merritt D., Navarro J. F., Ludlow A., Jenkins A., 2005, ApJ, 624, L85  
 Möller O., Kitzbichler M., Natarajan P., 2007, MNRAS, 379, 1195  
 Momcheva I., Williams K., Keeton C., Zabludoff A., 2006, ApJ, 641, 169  
 Morganti R. et al. 2006, MNRAS, 371, 157  
 Navarro J. F., Frenk C. S., White S. D. M., 1997, ApJ, 490, 493  
 Navarro J. F. et al. 2004, MNRAS, 349, 1039  
 Oguri M., 2007, New Journal of Physics, 9, 442  
 Oguri M., Keeton C. R., 2004, ApJ, 610, 663  
 Oguri M., Taruya A., Suto Y., Turner E. L., 2002, ApJ, 568, 488  
 Porciani C., Madau P., 2000, ApJ, 532, 679  
 Prugniel P., Simien F., 1997, A&A, 321, 111  
 Puchwein E., Bartelmann M., Dolag K., Meneghetti M., 2005, A&A, 442, 405  
 Read J. I., Trentham N., 2005, Royal Society of London Philosophical Transactions Series A, 363, 2693  
 Rozo E., Chen J., Zentner A. R., 2007, preprint (arXiv:0710.1683)  
 Rozo E., Nagai D., Keeton C., Kravtsov A., 2008, ApJ, 687, 22  
 Rusin D., Tegmark M., 2001, ApJ, 553, 709  
 Sellwood J. A., McGaugh S. S., 2005, ApJ, 634, 70  
 Sérsic J. L., 1968, Atlas de galaxias australes. Cordoba, Argentina: Observatorio Astronomico, 1968  
 Turner E. L., Ostriker J. P., Gott III J. R., 1984, ApJ, 284, 1  
 Wambsganss J., Ostriker J. P., Bode P., 2008, ApJ, 676, 753  
 Wyithe J. S. B., Turner E. L., Spergel D. N., 2001, ApJ, 555, 504  
 Young P., 1980, ApJ, 242, 1232

## APPENDIX A: VARIATION OF LENSING CROSS-SECTION WITH INNER SLOPE AND ORIENTATION

In Section 4.1, we quantified a selection bias based on dark matter halo inner slope using ratios

$$\langle R_{1,0.5}(N) \rangle = \frac{\langle \sigma_N(\gamma_{\text{dm}} = 1.0) \rangle}{\langle \sigma_N(\gamma_{\text{dm}} = 0.5) \rangle}, \quad (\text{A1})$$

where the averages indicate an average over orientations, and  $N$  can indicate either the total cross-section or the cross-section for some number of images  $N$ . We can also define a comparable quantity ( $\langle R_{1.5,1}(N) \rangle$ ) for  $\gamma_{\text{dm}} = 1.5$  versus  $\gamma_{\text{dm}} = 1$ . Ratios of one indicate an absence of selection bias, and we have generally found these ratios to be  $> 1$  (the strong-lensing cross-sections increase with  $\gamma_{\text{dm}}$ ).

We now address the question of whether these ratios are the same for each viewing direction, i.e. we consider

$$R_{1,0.5}(N, a'/a, b'/a) = \frac{\sigma_N(\gamma_{\text{dm}} = 1.0, a'/a, b'/a)}{\sigma_N(\gamma_{\text{dm}} = 0.5, a'/a, b'/a)} \quad (\text{A2})$$

and a comparable quantity  $R_{1.5,1}(N, a'/a, b'/a)$ . If these ratios stay (nearly) constant while changing  $a'/a$  and  $b'/a$ , then the selection bias with dark matter halo inner slope is not a (strong) function of viewing direction for galaxies with non-spherical shapes.

For the triaxial lower mass models, these ratios are indeed approximately constant (to within  $\sim 10$  per cent) for  $\sigma_{\text{tot}}$ ,  $\sigma_2$ , and  $\sigma_4$ , independent of magnification bias mode. For the triaxial higher mass model, where dark matter is more important, we find a stronger dependence on viewing direction. For  $\sigma_2$ , there are up to  $\sim 30$  per cent level trends for  $R_{1,0.5}$  and  $R_{1.5,1}$  to be lower (i.e., closer to unity and hence indicating less selection bias with  $\gamma_{\text{dm}}$ ), when viewing the model along the intermediate axis. This change occurs because in that orientation, the projected ellipticity and therefore  $\sigma_4$  is maximised, which decreases  $\sigma_2$  because 2-image systems can only occur outside of the tangential caustic. For  $\sigma_4$ , this is the case when viewing the model along the short axis (for  $R_{1,0.5}$ ) and along the long axis (for  $R_{1.5,1}$ ).

It is not clear that the details of this orientation-dependence of the selection bias with  $\gamma_{\text{dm}}$  is very important except for special situations. When analysing data from a

typical survey, we expect that galaxies are oriented randomly (before the imposition of strong lensing “orientation bias”), so the angle-averaged selection biases from Section 4.1 are the relevant quantities. We include the analysis here as an indication that if one isolates a special subset of strong lenses based on their projected shape, such as those for which the lens is particularly round or flattened, then the treatment of selection bias with  $\gamma_{\text{dm}}$  and possibly other properties must be specialised to that subset rather than using the orientation-averaged case.

## APPENDIX B: RELATIONSHIP BETWEEN DARK MATTER FRACTION AND EINSTEIN RADIUS

We seek to understand why the relation between dark matter fraction and Einstein radius shown in Fig. 8 is perfectly one-to-one. We begin with the Einstein radius definition,  $\bar{\kappa}(R_{\text{ein}}) = 1$ , meaning that the average convergence within the Einstein radius is unity (see also section 3.1 of paper I). Suppose the model has stellar and dark matter components. Then the definition of the Einstein radius is

$$\bar{\kappa}_{\text{tot}}(R_{\text{ein}}) = \bar{\kappa}_{\star}(R_{\text{ein}}) + \bar{\kappa}_{\text{dm}}(R_{\text{ein}}) = 1. \quad (\text{B1})$$

The stellar and dark matter mass fractions within the Einstein radius are, by definition,

$$f'_{\star}(R_{\text{ein}}) = \frac{\bar{\kappa}_{\star}(R_{\text{ein}})}{\bar{\kappa}_{\text{tot}}(R_{\text{ein}})}, \quad f'_{\text{dm}}(R_{\text{ein}}) = \frac{\bar{\kappa}_{\text{dm}}(R_{\text{ein}})}{\bar{\kappa}_{\text{tot}}(R_{\text{ein}})}. \quad (\text{B2})$$

Thus, equation (B1) can be rewritten as

$$f'_{\star}(R_{\text{ein}}) + f'_{\text{dm}}(R_{\text{ein}}) = 1 \quad (\text{B3})$$

On the one hand, this is entirely unsurprising: if the galaxy has stars and dark matter, the stellar and dark matter mass fractions must add up to unity. But on the other hand, this equation does illuminate our results in Fig. 8. Consider changing the dark matter component while keeping the stellar component fixed. As we vary the dark matter component, the Einstein radius will change. That in turn changes the first term in equation (B3), which necessarily changes the second term, too. However, if we hold the stellar component fixed, the first term is a function of a single variable, namely the Einstein radius. Since  $f'_{\text{dm}} = 1 - f'_{\star}$  that means the dark matter fraction can likewise depend only on a single variable,  $R_{\text{ein}}$ . In other words, if we hold the stellar component fixed, then no matter what we do to the dark matter component, the changes to  $f'_{\text{dm}}$  propagate only through the Einstein radius, and we have a perfect one-to-one correspondence between  $R_{\text{ein}}$  and  $f'_{\text{dm}}$ .